High-order discretization of a gyrokinetic Vlasov model in edge plasma geometry

Milo R. Dorr [a],[*], Phillip Colella [c], Mikhail A. Dorf [b], Debojyoti Ghosh [a], Jeffrey A.F. Hittinger [a], Peter O. Schwartz [c]

[a] *Center for Applied Scientific Computing, Lawrence Livermore National Laboratory, 7000 East Avenue L-561, Livermore, CA 94550, United States of America* [1]
[b] *Fusion Energy Program, Lawrence Livermore National Laboratory, 7000 EastAvenue L-630, Livermore, CA 94550, United States of America*
[c] *Applied Numerical Algorithms Group, Lawrence Berkeley National Laboratory, One Cyclotron Road Mail Stop 50A-1148, Berkeley, CA 94720, United States of America* [2]

ARTICLE INFO

ABSTRACT

We describe a new spatial discretization of a continuum gyrokinetic Vlasov model in axisymmetric tokamak edge plasma geometries. The geometries are represented using a multiblock decomposition in which logically distinct blocks are smoothly mapped from rectangular computational domains and are aligned with magnetic flux surfaces to accommodate strong anisotropy induced by the magnetic field. We employ a fourth-order, finite-volume discretization in mapped coordinates to mitigate the computational expense associated with discretization on 4D phase space grids. Applied to a conservative formulation of the gyrokinetic system, a finite-volume approach expresses local conservation discretely in a natural manner involving the calculation of normal fluxes at cell faces. In the approach presented here, the normal fluxes are computed in terms of face-averaged velocity normals in such a way that (*i*) the divergence-free property of the gyrokinetic velocity is preserved discretely to machine precision, (*ii*) the configuration space normal velocities are independent of mapping metrics, and (*iii*) the configuration space normal velocities are computed from exact pointwise evaluation of magnetic field data except for one term. The algorithms described in this paper form the foundation of a continuum gyrokinetic edge code named COGENT, which is used here to perform a convergence study verifying the accuracy of the spatial discretization.

© 2018 Elsevier Inc. All rights reserved.

1. Introduction

In this paper, we describe a new approach for the spatial discretization of a continuum kinetic model of plasma evolution in the edge region of a tokamak fusion reactor. The development of a complete edge plasma simulation capability is a significant undertaking involving many components. Among these is the ability to model the phase space advection of
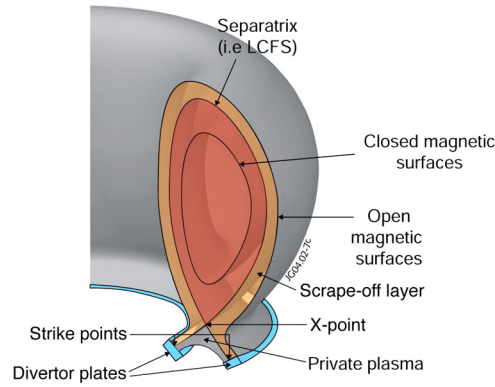

Fig. 1. Edge geometry schematic [1]. The edge region is defined from the outer wall, where field lines terminate at the divertor plates or at the wall, across the magnetic separatrix and into the core region of closed, concentric flux surfaces.
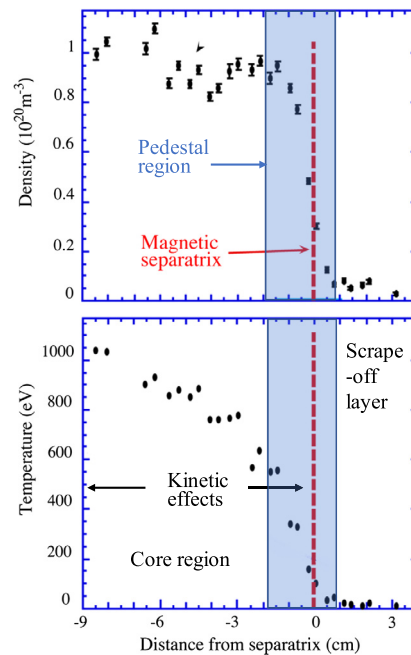

Fig. 2. Plasma density and temperature measured in the DIII-D tokamak [39]. The region of rapid transition occurring near the separatrix is known as the pedestal.

plasma species distribution functions in a configuration space domain spanning both sides of the magnetic separatrix. Our focus here is on the discretization of a continuum Vlasov operator in such geometries, addressing numerical challenges including high-dimensionality, strong anisotropy and the preservation of solution constraints.

As shown schematically in Fig. 1, the edge region of a tokamak encompasses part of the core region, part or all of the region between the plasma and the reactor wall, and the divertor plates. In addition to geometric complexity, an important feature that distinguishes the edge from the core is the development of a region of steep gradients in the density and temperature profiles called the pedestal (Fig. 2), the height of which determines the quality of plasma confinement, and hence fusion gain. A kinetic plasma model is needed in this region, because the radial width of the pedestal observed in experiments is comparable to the radial width of individual particle orbits (leading to large distortions of the local distribution functions from a Maxwellian), while the mean free path can be comparable to the scale length for temperature variations along the magnetic field (violating the assumptions underlying a collisional fluid model).

Because of the large number of independent variables in a fully kinetic model, as well as the fast time scale represented by the ion gyrofrequency, gyrokinetic models have been developed that remove the fast gyromotion asymptotically and thereby facilitate numerical treatments. Continuum models consist of a Vlasov operator describing the evolution of plasma species distribution functions in a particular coordinate system combined with some variant of Maxwell's equations and collision terms. Codes such as GENE [29,30], GS2 [16,36] and GYRO [4–6] have been successfully employed to model core plasmas for many years. These codes exploit the opportunity to express distribution functions as perturbations δf about a
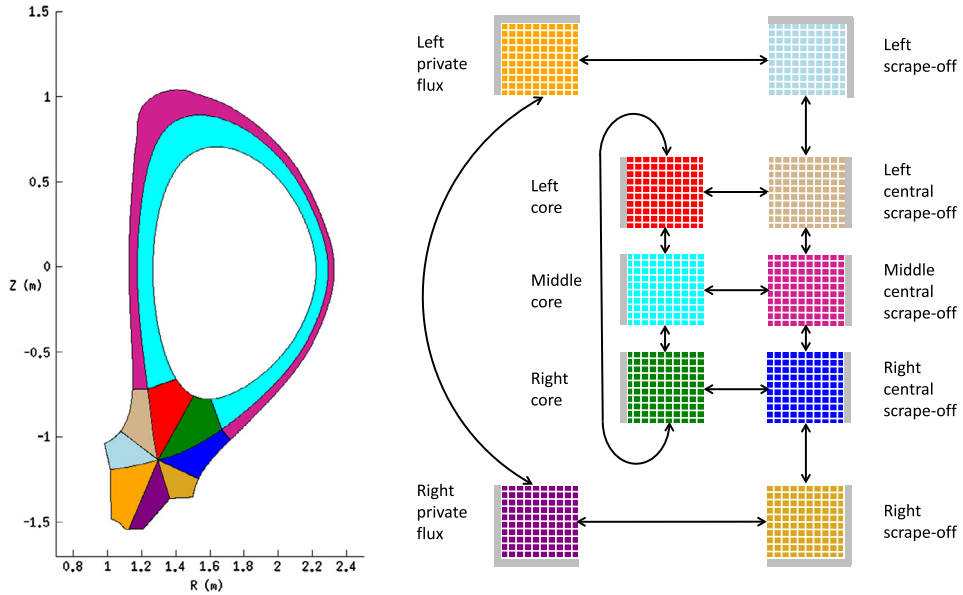
Fig. 3. Mapped multiblock decomposition of the edge geometry (left) and the corresponding locally rectangular computational domain (right). The arrows indicate the inter-block connectivity, and the gray regions indicate physical boundaries.

known Maxwellian distribution f_0. Since edge plasma distributions can deviate significantly from Maxwellian, it is unclear how to extend such perturbative approaches into this region. Consequently, in recent years there has been growing interest in *full-f* methods that evolve the entire distribution function in gyrokinetic models using both particle-based [7,24,28,33,34, 37] and continuum [21,26,27] methods. Another challenge faced by edge models that has caused their development to lag that of flux-tube or global core codes is the need to address additional geometric complexity resulting from the inclusion of both sides of the magnetic separatrix, spanning regions of both closed and open field lines.

In this paper, we describe an approach for the discretization of a continuum full-*f*, gyrokinetic Vlasov system in axisymmetric edge geometries. The system is treated as a conservation law describing the advection of plasma species distribution functions in a four dimensional phase space (2 configuration space and 2 velocity space coordinates). A (mostly) flux-surface-aligned, mapped-multiblock (MMB) coordinate system (Fig. 3) is used to accommodate strong anisotropy in the direction of magnetic field lines, similar to fluid edge codes such as UEDGE [40–42] and SOLPS-ITER [45]. We formulate a high-order spatial discretization to reduce the phase space grid size needed for a specific level of accuracy relative to a lower-order approximation, as well as to reduce numerical dissipation in long-time integrations. In particular, we employ a semi-discretization based on a general formalism [8,38] for the creation of arbitrarily high-order finite-volume spatial discretizations in mapped coordinates. This formalism is summarized in Sections 3.1 and 3.3. A unique feature of the edge geometry application is that a key requirement of the formalism, namely, that the block mappings are smooth up to and some distance beyond block boundaries, cannot be satisfied by a completely flux-surface-aligned mapping due to the singularity of the metric factors at the X point, where the magnetic separatrix intersects itself and the poloidal field component vanishes. As discussed in Section 4, some dealignment is therefore necessary in a neighborhood of the X point to enable high-order differentiation there.

Since the phase space velocity in gyrokinetic models is developed via Hamiltonian equations of motion, the zero velocity divergence implied by the area-preserving property of such dynamical systems is an important constraint that must be maintained during discretization to avoid the accumulation of truncation error in long-time integrations. For the gyrokinetic model [22] addressed here and presented in Section 2, we demonstrate in Section 3.2 how the divergence-free property can be satisfied to machine precision in the context of our high-order, MMB, finite-volume discretization. Specifically, in calculating the phase space cell averages of the gyrokinetic flux divergence, the velocity enters through integrals of the normal components over the cell faces, which in turn are used to compute flux normals via a high-order product formula. By exploiting the fact that the phase space velocity can be written as a sum of vectors including a certain skew-symmetric, second-order tensor divergence, Stokes' theorem can be invoked to reduce the cell face velocity integrals to face boundary integrals that telescopically sum to zero in the cell-averaged finite volume divergence calculation. Additional benefits accrue from the fact that the face boundary integrals corresponding to three of the four velocity terms (*i.e.*, parallel streaming, curvature and ∇B drifts) are computed exactly, and no metric factors appear.

The algorithms described herein provide the foundation of the COGENT (COntinuum Gyrokinetic Edge New Technology) code, which we have been developing for the solution of continuum gyrokinetic models in multiblock geometries, including those describing the tokamak edge. An overview of COGENT is the topic of Section 5, and in Section 6, we utilize COGENT to demonstrate the accuracy of the spatial discretization described in the preceding sections. The efficient discretization of

the gyrokinetic Vlasov operator is necessary but not sufficient for the complete simulation of the edge plasma problem. Given its fundamental importance, however, we have limited the scope of this paper to only that part. As described in Section 5, COGENT includes a number of the other components (*e.g.*, collision operators, self-consistent electrostatic fields and high-order semi-explicit time integration methods) needed to address edge-relevant problems, which have been used in several verification studies [10,12–15,17,19]. These additional components have all been compatibly developed using the same high-order, finite-volume formalism underlying the Vlasov term treatment described herein. To our knowledge, COGENT's ability to solve a continuum gyrokinetic model in edge geometries spanning both sides of the magnetic separatrix is unique.

2. The gyrokinetic Vlasov system

We target a reduced version of the collisionless full-f gyrokinetic model of [22]:

$$\frac{\partial (B_\parallel^* f)}{\partial t} + \nabla_{\mathbf{R}} \cdot \left(\dot{\mathbf{R}} B_\parallel^* f \right) + \frac{\partial}{\partial v_\parallel} \left(\dot{v}_\parallel B_\parallel^* f \right) = 0, \tag{1}$$

where

$$\dot{\mathbf{R}} = \dot{\mathbf{R}}(\mathbf{R}, v_\parallel, \mu, t) = \frac{v_\parallel}{B_\parallel^*} \mathbf{B}^* + \frac{\rho_L}{Z B_\parallel^*} \mathbf{b} \times \mathbf{G}, \tag{2a}$$

$$\dot{v}_\parallel = \dot{v}_\parallel(\mathbf{R}, v_\parallel, \mu, t) = -\frac{1}{m B_\parallel^*} \mathbf{B}^* \cdot \mathbf{G}, \tag{2b}$$

and

$$\mathbf{B}^* = \mathbf{B}^*(\mathbf{R}, v_\parallel) = \mathbf{B} + \rho_L \frac{m v_\parallel}{Z} \nabla_{\mathbf{R}} \times \mathbf{b}, \tag{3a}$$

$$B_\parallel^* = B_\parallel^*(\mathbf{R}, v_\parallel) = \mathbf{b} \cdot \mathbf{B}^*, \tag{3b}$$

$$\mathbf{G} = \mathbf{G}(\mathbf{R}, \mu, t) = Z \nabla_{\mathbf{R}} \Phi + \frac{\mu}{2} \nabla_{\mathbf{R}} B. \tag{3c}$$

The unknown quantity $f = f(\mathbf{R}, v_\parallel, \mu, t)$ is the plasma species distribution function in gyrocenter phase space coordinates $(\mathbf{R}, v_\parallel, \mu)$, which are described further below and whose equations of motion are given by (2)–(3). B and $\mathbf{b}$ are the magnitude and direction of the magnetic field $\mathbf{B} = B\mathbf{b}$, respectively. Z and m are the species charge state and mass, respectively. Φ is the electric potential. For our present purposes, we assume the long wavelength limit in which the Larmor radius is much smaller than the characteristic length scales for electrostatic potential variations. We utilize a particular normalization described in Appendix A.1 that nondimensionalizes all quantities, including the Larmor number, ρ_L, defined in Table 5.

Gyrocenter coordinates play a key role in gyrokinetic models in two important ways. First, they reduce what would otherwise be a six-dimensional phase space to five dimensions: $\mathbf{R}$ is the three-dimensional configuration space coordinate, $v_\parallel$ is the velocity space component along field lines, and the magnetic moment $\mu = m v_\perp^2 / 2B$ is related to the velocity $v_\perp$ perpendicular to field lines. Through the use of asymptotic orderings, gyrocenter coordinates are specifically constructed so as to make the distribution function f independent of the gyrophase. The latter component, which would have been the third velocity component, can then be ignored. The magnetic moment μ, an adiabatic invariant, is assumed to be constant in the development of gyrokinetic theories, which is why no evolution equation appears for it. The second benefit of gyrocenter coordinates is that the gyromotion is removed, which would otherwise represent a fast time scale that would need to be resolved.

The gyrokinetic phase space velocity (2) models strong flow along magnetic field lines, represented by the $v_\parallel \mathbf{B}$ quantity, together with curvature, ∇B and $\mathbf{E} \times \mathbf{B}$ drift terms containing the ρ_L factor, which is assumed small in the gyrokinetic asymptotic ordering. For typical tokamak parameters, the difference in the magnitude of the streaming and drift terms can be a few orders of magnitude. The resulting strong anisotropy resulting from the disparity in parallel and perpendicular quantities has many implications in the development of numerical algorithms. Because gyrocenter coordinates are developed as a Hamiltonian dynamical system, the velocity (2) satisfies the area preserving property

$$\nabla_{\mathbf{R}} \cdot \left(B_\parallel^* \dot{\mathbf{R}} \right) + \frac{\partial}{\partial v_\parallel} \left(B_\parallel^* \dot{v}_\parallel \right) = 0, \tag{4}$$

where $B_\parallel^*$ is the Jacobian of the mapping between lab frame and gyrocenter coordinates. The analytic verification of (4) is contained in Appendix A.2. As noted in [22], the gyrokinetic Vlasov equation can therefore be expressed in either convective or conservative form. We choose the latter with the objective of achieving a correspondingly conservative numerical discretization. The potential Φ in (3c) is evaluated by solving some form of Maxwell's equations. For the purposes of this paper, we assume that Φ is known, although the COGENT code used for our numerical example includes additional options, as discussed in Section 5.

The gyrokinetic system is posed in a domain defined by the tokamak magnetic geometry, which is comprised of field lines lying on concentric flux surfaces (Fig. 1). In this paper, we assume an axisymmetric geometry, where all quantities are assumed to be constant in the toroidal direction. The configuration space domain therefore consists of a single poloidal slice. Due to large variations of plasma parameters along and across field lines (and therefore along and across sliced flux surfaces in the poloidal plane), there is strong motivation to discretize in coordinates where at least one of the coordinate directions is defined by the flux surfaces. Since a single, smooth, flux-surface-aligned coordinate mapping cannot be constructed over the entire domain, we consider a multiblock decomposition such as the one depicted in the left-hand side of Fig. 3. This decomposition is constructed by first recognizing the natural partitioning defined by the magnetic separatrix into the core, scrape-off and private flux regions. Each region is further decomposed into blocks such that (*i*) each block can be mapped from a logically rectangular computational domain and (*ii*) adjacent blocks must abut along entire boundaries. The core region is therefore subdivided into the left (LCORE), middle (MCORE) and right (RCORE) blocks; the scrape-off layer is decomposed into the left (LSOL), left-central (LCSOL), middle-central (MCSOL), right-central (RCSOL) and right (RSOL) blocks, and the private flux region is decomposed into the left (LPF) and right (RPF) blocks. The right-hand side of Fig. 3 depicts the inter-block connectivity in the mapped coordinate domain. Within each mapped block, rectangular grids are introduced, resulting in a block rectilinear gridding of the physical domain. We require that the grids be conformal across inter-block boundaries, but otherwise no additional grid smoothness across block boundaries is assumed. For parallelization purposes, the rectangular block grids are further decomposed, load balanced and assigned to processors in a fully general manner.

Although the multiblock decomposition rules imposed above could have been satisfied using only six blocks by combining the LCORE, MCORE and RCORE blocks into a single block and the LCSOL, MCSOL and RCSOL blocks into another block, the generation of smooth mappings on the resulting "long and skinny" merged blocks is non-trivial. The advantage of the ten-block decomposition shown in Fig. 3 is that eight of the blocks are curvilinear quadrilaterals that are relatively modest deformations of the unit square; the MCORE and MCSOL blocks can be mapped to the unit square using nearly polar coordinate transformations.

On this mapped multiblock grid, we consider the discretization of the system (1)–(3). Among our requirements is the discrete enforcement of the zero velocity divergence condition (4) assumed in the conservative formulation. A second requirement is high-order (*i.e.*, greater than second-order) accuracy, which reduces the number of phase space degrees of freedom to achieve a given level of accuracy. A high-order method is also important for reducing numerical dissipation in long-time integrations. We therefore begin with a review of a general approach [8] for constructing fourth-order, finite-volume discretizations of hyperbolic conservation laws in mapped coordinates on a single block. In this context, we then describe the calculation of the gyrokinetic velocities in the mapped coordinate system such that the divergence free condition (4) is satisfied to machine precision. In our finite volume approach, the mapped grid normal velocities are used in flux calculations on cell faces together with discretized distribution functions. On cell faces near interblock boundaries, calculation of the latter is accomplished using suitably high-order interpolation [38], enabling the extension of the discretization to multiblock geometries such as the edge geometry in Fig. 3.

3. Phase space discretization

Fundamental to our approach is a general strategy for the systematic development of high-order, finite-volume discretizations in mapped coordinates. Additional details are contained in [8].

3.1. Fourth-order, finite-volume discretization in a mapped block

Consider a smooth mapping $\mathbf{X}$ from the unit cube onto the spatial domain Ω:

$$\mathbf{X} = \mathbf{X}(\boldsymbol{\xi}), \ \mathbf{X} : [0, 1]^D \rightarrow \Omega.$$

Given this mapping, the divergence of a vector field on Ω can be written in terms of derivatives in $[0, 1]^D$, which will serve as our computational domain. That is,

$$\nabla_{\mathbf{X}} \cdot \mathbf{F} = J^{-1} \nabla_{\boldsymbol{\xi}} \cdot (\mathbf{N}^T \mathbf{F}), \tag{5a}$$

$$J = \det\left(\frac{\partial \mathbf{X}}{\partial \boldsymbol{\xi}}\right), \ \ (\mathbf{N}^T)_{d,d'} = \det\left(R_d\left(\frac{\partial \mathbf{X}}{\partial \boldsymbol{\xi}}, \mathbf{e}^{d'}\right)\right), \ 1 \leq d, d' \leq D, \tag{5b}$$

where $R_d(\mathbf{M}, \mathbf{v})$ denotes the matrix obtained by replacing the dth row of the matrix $\mathbf{M}$ by the vector $\mathbf{v}$, and $\mathbf{e}^d$ denotes the unit vector in the d-th coordinate direction.

In a finite volume approach, Ω is discretized as a union of control volumes. For Cartesian grid finite volume methods, a control volume $W_{\mathbf{i}}$ takes the form

$$W_{\mathbf{i}} = [\mathbf{i}h, (\mathbf{i} + \mathbf{u})h], \ \mathbf{i} \in \mathbb{Z}^D, \ \mathbf{u} = (1, 1, \ldots, 1),$$

where h is the grid spacing. When using mapped coordinates, we define control volumes in Ω as the images $\mathbf{X}(W_\mathbf{i})$ of the cubic control volumes $W_\mathbf{i} \subset [0, 1]^D$. Then, by changing variables and applying the divergence theorem, we obtain the flux divergence integral over a physical control volume $\mathbf{X}(W_\mathbf{i})$ by

$$\int\limits_{\mathbf{X}(W_\mathbf{i})} \nabla_\mathbf{x} \cdot \mathbf{F} d\mathbf{x} = \int\limits_{W_\mathbf{i}} \nabla_\xi \cdot (\mathbf{N}^T \mathbf{F}) d\xi = \sum_{d=0}^{D-1} \sum_{\alpha=0}^{1} (-1)^{\alpha+1} \int\limits_{V_d^\alpha} (\mathbf{N}^T \mathbf{F})_d dV_\xi, \tag{6}$$

where the V_d^0 and V_d^1 are lower and upper faces of cell $W_\mathbf{i}$ in the d-th direction, respectively. As described in [8], the integrals on the cell faces V_d^α can be approximated using the following formula for the average of a product in terms of fourth-order accurate face averages of each factor:

$$\langle ab \rangle_{\mathbf{i}+\frac{1}{2}\mathbf{e}^d} = \langle a \rangle_{\mathbf{i}+\frac{1}{2}\mathbf{e}^d} \langle b \rangle_{\mathbf{i}+\frac{1}{2}\mathbf{e}^d} + \frac{h^2}{12} \mathbf{G}_0^{\perp,d} \left(\langle a \rangle_{\mathbf{i}+\frac{1}{2}\mathbf{e}^d} \right) \cdot \mathbf{G}_0^{\perp,d} \left(\langle b \rangle_{\mathbf{i}+\frac{1}{2}\mathbf{e}^d} \right) + O(h^4). \tag{7}$$

Here, $\mathbf{G}_0^{\perp,d}$ is the second-order accurate central difference approximation to the component of the gradient operator orthogonal to the d-th direction: $\mathbf{G}_0^{\perp,d} \approx \nabla_\xi - \mathbf{e}^d \frac{\partial}{\partial \xi_d}$, and the operator $\langle \cdot \rangle_{\mathbf{i}+\frac{1}{2}\mathbf{e}^d}$ denotes a fourth-order accurate average over the cell face centered at $\mathbf{i} + \frac{1}{2}\mathbf{e}^d$:

$$\langle q \rangle_{\mathbf{i}+\frac{1}{2}\mathbf{e}^d} = \frac{1}{h^{D-1}} \int\limits_{V_d^\alpha} q dV_\xi + O(h^4).$$

Alternative expressions to (7) are obtained by replacing the averages $\langle a \rangle_{\mathbf{i}+\frac{1}{2}\mathbf{e}^d}$ and/or $\langle b \rangle_{\mathbf{i}+\frac{1}{2}\mathbf{e}^d}$ used in the transverse gradients $\mathbf{G}_0^{\perp,d}$ by the corresponding face-centered pointwise values $a_{\mathbf{i}+\frac{1}{2}\mathbf{e}^d}$ and/or $b_{\mathbf{i}+\frac{1}{2}\mathbf{e}^d}$, respectively.

When applied in the discretization of the phase space divergence operator in the gyrokinetic system (1), we consider the flux $\mathbf{F} = f\mathbf{u}$, where

$$\mathbf{u} = (u_0, u_1, u_2, u_3) = (u_{v_\parallel}, \mathbf{u_R}) = (B_\parallel^* \dot{v}_\parallel, B_\parallel^* \dot{\mathbf{R}}). \tag{8}$$

We therefore obtain

$$\int\limits_{\mathbf{X}(W_\mathbf{i})} \nabla_\mathbf{x} \cdot \mathbf{F} d\mathbf{x} = h^3 \sum_{d=0}^{3} \sum_{\alpha=0}^{1} (-1)^{\alpha+1} F_{\mathbf{i}\pm\frac{1}{2}\mathbf{e}^d}^d + O(h^4), \tag{9}$$

where, taking $(\mathbf{N}^T \mathbf{u})_d$ and f as the factors in the product formula (7),

$$F_{\mathbf{i}\pm\frac{1}{2}\mathbf{e}^d}^d = \left\langle (\mathbf{N}^T \mathbf{u})_d \right\rangle_{\mathbf{i}+\frac{1}{2}\mathbf{e}^d} \langle f \rangle_{\mathbf{i}+\frac{1}{2}\mathbf{e}^d} + \frac{h^2}{12} \left(\mathbf{G}_0^{\perp,d} \left\langle (\mathbf{N}^T \mathbf{u})_d \right\rangle_{\mathbf{i}+\frac{1}{2}\mathbf{e}^d} \right) \cdot \left(\mathbf{G}_0^{\perp,d} (\langle f \rangle_{\mathbf{i}+\frac{1}{2}\mathbf{e}^d}) \right). \tag{10}$$

We note that an alternative discretization can be obtained by preserving the flux $\mathbf{F}$ as one of the product formula factors, yielding

$$F_{\mathbf{i}\pm\frac{1}{2}\mathbf{e}^d}^d = \sum_{s=0}^{3} \langle N_d^s \rangle_{\mathbf{i}+\frac{1}{2}\mathbf{e}^d} \langle F^s \rangle_{\mathbf{i}+\frac{1}{2}\mathbf{e}^d} + \frac{h^2}{12} \sum_{s=0}^{3} \left(\mathbf{G}_0^{\perp,d} \langle N_d^s \rangle_{\mathbf{i}+\frac{1}{2}\mathbf{e}^d} \right) \cdot \left(\mathbf{G}_0^{\perp,d} (\langle F^s \rangle_{\mathbf{i}+\frac{1}{2}\mathbf{e}^d}) \right), \tag{11}$$

where F^s is the s-th component of $\mathbf{F}$ and N_d^s is the (s, d)-th element of the matrix $\mathbf{N}$. In [8], it is demonstrated that the computation of the face averages $\langle N_d^s \rangle_{\mathbf{i}+\frac{1}{2}\mathbf{e}^d}$ can be reduced to integrals over cell edges. Moreover, assuming that the edge integrals are performed with the same quadratures wherever they appear,

$$\sum_{d=0}^{3} \sum_{\alpha=0}^{1} (-1)^{\alpha+1} \int\limits_{V_d^\alpha} N_d^s dV_\xi = 0, \tag{12}$$

which guarantees the freestream property that the divergence of a constant vector field computed by (6) is identically zero. Free-stream preservation is an extremely important property in the simulation of flows using mapped coordinate systems, since it represents a constraint on the approximation of the metric terms that reduces the dependence of computed solutions on the choice of mapping and metric discretization [35]. However, as will be demonstrated in the next section, the factorization (10) enables a discretization in which the divergence of the gyrokinetic velocity $\mathbf{u}$ vanishes to machine precision, thereby enforcing the assumption (4) made in the conservative formulation (1). Moreover, the formulation is free of discretized metric terms, which naturally achieves one of the goals addressed in free-stream preserving approaches.

Calculation of the face-averaged fluxes (10) is therefore reduced to the calculation of face-averaged distribution functions and mapped normal velocity components. One choice for the former is obtained from the fourth-order, centered-difference formula

$$\langle f \rangle_{\mathbf{i}+\frac{1}{2}\mathbf{e}^d} = \frac{7}{12}\left(\bar{f}_{\mathbf{i}} + \bar{f}_{\mathbf{i}+\mathbf{e}^d}\right) - \frac{1}{12}\left(\bar{f}_{\mathbf{i}+2\mathbf{e}^d} + \bar{f}_{\mathbf{i}-\mathbf{e}^d}\right) + O(h^4),$$ (13)

where $\bar{f}_{\mathbf{i}}$ denotes the average of f on cell $\mathbf{i}$. This results in a dissipationless scheme to which a limiter can also be added. Alternatively, an upwind method with order higher than four, such as the fifth-order WENO scheme [31], may be employed. Boundary conditions are also implemented here through the setting of inflow conditions in physical boundary ghost cells. Fourth-order face averages of the mapped normal velocity components can be computed directly from (2) using the product formula (7) and metric factor face averages, but as shown in the next section, a more careful exploitation of the specific structure of the gyrokinetic velocity results in a discretization that is also discretely divergence free.

3.2. Gyrokinetic velocity discretization

As shown in Appendix A.2, the divergence of the gyrokinetic velocity (2) is zero. In this section, we demonstrate how to preserve this property when computing the divergence using the mapped-grid, finite-volume discretization described in the preceding section. Specifically, we show how the mapped normal velocity components $\langle(\mathbf{N}^T\mathbf{u})_d\rangle_{\mathbf{i}+\frac{1}{2}\mathbf{e}^d}$ can be computed such that the divergence integral (6) with $\mathbf{F} = \mathbf{u}$ is zero to machine precision.

Let $\mathbf{A}$ denote a magnetic potential (*i.e.*, $\mathbf{B} = \nabla_{\mathbf{R}} \times \mathbf{A}$) and let

$$p = \rho_L\left(\Phi + \frac{\mu B}{2Z}\right).$$ (14)

Letting $(x_0, x_1, x_2, x_3) = (v_\parallel, \mathbf{R})$, we define

$$\widetilde{\mathbf{u}} = \mathbf{u} - \widehat{\mathbf{u}},$$ (15)

where $\widehat{\mathbf{u}} = (\widehat{\mathbf{u}}_j)$ is the vector with entries

$$\widehat{\mathbf{u}}_j = -\delta_{0,j}\frac{Z}{m\rho_L}\mathbf{B} \cdot \nabla_{\mathbf{R}}p, \qquad 0 \le j \le 3.$$ (16)

$\widehat{\mathbf{u}}$ is divergence-free, and therefore so is $\widetilde{\mathbf{u}}$. Using the components of $\widetilde{\mathbf{u}} = (\widetilde{u}_0, \widetilde{u}_1, \widetilde{u}_2, \widetilde{u}_3)$, we define the 3-form

$$\boldsymbol{\sigma} = \widetilde{u}_3\, dx_0 \wedge dx_1 \wedge dx_2 - \widetilde{u}_2\, dx_0 \wedge dx_1 \wedge dx_3 + \widetilde{u}_1\, dx_0 \wedge dx_2 \wedge dx_3 - \widetilde{u}_0\, dx_1 \wedge dx_2 \wedge dx_3.$$ (17)

The mapped normal velocity components of $\widetilde{\mathbf{u}}$ can be expressed (see Appendix A.3) in terms of surface integrals of $\boldsymbol{\sigma}$ using the parameterization given by our mapping $\mathbf{X}$ (which implies a particular surface orientation that has already been accounted for in (6)) as

$$\int_{V_d^\alpha} (\mathbf{N}^T\widetilde{\mathbf{u}})_d\, d\mathbf{V}_{\boldsymbol{\xi}} = (-1)^{d+1}\int_{\mathbf{X}(V_d^\alpha)} \boldsymbol{\sigma}, \qquad 0 \le d \le 3.$$ (18)

Since $\widetilde{\mathbf{u}}$ is divergence-free, the exterior derivative $d\boldsymbol{\sigma}$ is zero. Poincaré's Lemma (applied on the contractible manifolds $\mathbf{X}(V_d^\alpha)$) therefore ensures the existence of a 2-form

$$\boldsymbol{\omega} = \sum_{0 \le i < i' \le 3} \omega_{i,i'}\, dx_i \wedge dx_{i'}$$ (19)

such that $\boldsymbol{\sigma} = d\boldsymbol{\omega}$. It therefore follows that

$$\widetilde{\mathbf{u}}_j = \sum_{j'=0}^{3} \frac{\partial \zeta_{j,j'}}{\partial x_{j'}}, \qquad 0 \le j \le 3,$$ (20)

where

$$\boldsymbol{\zeta} = (\zeta_{i,j}) = \begin{pmatrix} 0 & -\omega_{0,1} & \omega_{0,2} & -\omega_{0,3} \\ \omega_{0,1} & 0 & -\omega_{1,2} & \omega_{1,3} \\ -\omega_{0,2} & \omega_{1,2} & 0 & -\omega_{2,3} \\ \omega_{0,3} & -\omega_{1,3} & \omega_{2,3} & 0 \end{pmatrix}.$$ (21)

The form $\boldsymbol{\omega}$ is not unique. As described in Appendix A.4, particular $\omega_{i,j}$ satisfying (20)–(21) can be found by a careful inspection of $\widetilde{\mathbf{u}}$, yielding

$$\omega_{0,j} = (-1)^{j+1} v_{\parallel} (\mathbf{b} \times \nabla_{\mathbf{R}} p)_j, \quad 1 \leq j \leq 3, \tag{22a}$$

$$\omega_{1,2} = -v_{\parallel} \left(\mathbf{A} + \frac{m v_{\parallel} \rho_L}{Z} \mathbf{b} \right)_3, \tag{22b}$$

$$\omega_{1,3} = -v_{\parallel} \left(\mathbf{A} + \frac{m v_{\parallel} \rho_L}{Z} \mathbf{b} \right)_2, \tag{22c}$$

$$\omega_{2,3} = -v_{\parallel} \left(\mathbf{A} + \frac{m v_{\parallel} \rho_L}{Z} \mathbf{b} \right)_1, \tag{22d}$$

$$\omega_{i,j} = -\omega_{j,i}, \quad 0 \leq j < i \leq 3. \tag{22e}$$

Next, letting $\mathbf{X}^*$ denote the pullback mapping [2] defined by $\mathbf{X}$, we apply Stokes' theorem [43] to obtain

$$\int_{\mathbf{X}(V_d^{\alpha})} \boldsymbol{\sigma} = \int_{V_d^{\alpha}} \mathbf{X}^*(d\boldsymbol{\omega}) = \int_{V_d^{\alpha}} d(\mathbf{X}^*\boldsymbol{\omega}) = \sum_{d' \neq d} \sum_{\beta=0,1} (-1)^{d'+1+\beta} \int_{A_{d,d'}^{\alpha,\beta}} \mathbf{X}^*\boldsymbol{\omega}, \tag{23}$$

where $A_{d,d'}^{\alpha,0}$ and $A_{d,d'}^{\alpha,1}$ are the low and high side faces of V_d^{α} in direction d', respectively. The pullback form is defined by

$$\mathbf{X}^*\boldsymbol{\omega} = \sum_{0 \leq i < i' \leq 3} \sum_{0 \leq j < j' \leq 3} \omega_{i,i'} \det \begin{vmatrix} \frac{\partial X_i}{\partial \xi_j} & \frac{\partial X_i}{\partial \xi_{j'}} \\ \frac{\partial X_{i'}}{\partial \xi_j} & \frac{\partial X_{i'}}{\partial \xi_{j'}} \end{vmatrix} d\boldsymbol{\xi}_j \wedge d\boldsymbol{\xi}_{j'}. \tag{24}$$

In terms of coordinates, the pullback integrals are then [2]

$$\int_{A_{d,d'}^{\alpha,\beta}} \mathbf{X}^*\boldsymbol{\omega} = \sum_{\substack{0 \leq j < j' \leq 3 \\ j,j' \neq d,d'}} \sum_{0 \leq i < i' \leq 3} \int_{A_{d,d'}^{\alpha,\beta}} \omega_{i,i'} \det \begin{vmatrix} \frac{\partial X_i}{\partial \xi_j} & \frac{\partial X_i}{\partial \xi_{j'}} \\ \frac{\partial X_{i'}}{\partial \xi_j} & \frac{\partial X_{i'}}{\partial \xi_{j'}} \end{vmatrix} d\boldsymbol{\xi}_j d\boldsymbol{\xi}_{j'}. \tag{25}$$

For example, consider a cylindrical coordinate mapping of the form:

$$X_0 = v_{\parallel}(\xi_0), \tag{26a}$$

$$X_1 = R(\xi_1, \xi_2) \cos(\xi_3), \tag{26b}$$

$$X_2 = R(\xi_1, \xi_2) \sin(\xi_3), \tag{26c}$$

$$X_3 = Z(\xi_1, \xi_2), \tag{26d}$$

where $\xi_n^0 \leq \xi_n \leq \xi_n^1$ for $0 \leq n \leq 2$ and $0 \leq \xi_3 \leq 2\pi$. The evaluation of (25) yields

$$\int_{A_{d,d'}^{\alpha,\beta}} \mathbf{X}^*\boldsymbol{\omega} = Q_{d,d'}^{\alpha,\beta}, \tag{27}$$

where,

$$Q_{0,1}^{\alpha,\beta} = 2\pi \rho_L \int_{\xi_2^0}^{\xi_2^1} \left\{ \left[\left(-\eta_0^{\alpha} (\mathbf{b} \times \mathbf{E})_Z + \frac{\eta_1^{\alpha}}{2Z} (\mathbf{b} \times \nabla B)_Z \right) \frac{\partial R}{\partial \xi_2} \right. \right. \tag{28a}$$

$$\left. \left. + \left(\eta_0^{\alpha} (\mathbf{b} \times \mathbf{E})_R - \frac{\eta_1^{\alpha}}{2Z} (\mathbf{b} \times \nabla B)_R \right) \frac{\partial Z}{\partial \xi_2} \right] R \right\}_{\xi_1 = \xi_1^{\beta}} d\boldsymbol{\xi}_2, \tag{28b}$$

$$Q_{0,2}^{\alpha,\beta} = 2\pi \rho_L \int_{\xi_1^0}^{\xi_1^1} \left\{ \left[\left(-\eta_0^{\alpha} (\mathbf{b} \times \mathbf{E})_Z + \frac{\eta_1^{\alpha}}{2Z} (\mathbf{b} \times \nabla B)_Z \right) \frac{\partial R}{\partial \xi_1} \right. \right. \tag{28c}$$

$$\left. \left. + \left(\eta_0^{\alpha} (\mathbf{b} \times \mathbf{E})_R - \frac{\eta_1^{\alpha}}{2Z} (\mathbf{b} \times \nabla B)_R \right) \frac{\partial Z}{\partial \xi_1} \right] R \right\}_{\xi_2 = \xi_2^{\beta}} d\boldsymbol{\xi}_1, \tag{28d}$$

$$Q_{0,3}^{\alpha,\beta} = \rho_L \int_{\xi_1^0}^{\xi_1^1} \int_{\xi_2^0}^{\xi_2^1} \left[-\eta_0^{\alpha} (\mathbf{b} \times \mathbf{E})_{\Phi} + \frac{\mu \eta_1^{\alpha}}{2Z} (\mathbf{b} \times \nabla B)_{\Phi} \right] \left(\frac{\partial R}{\partial \xi_2} \frac{\partial Z}{\partial \xi_1} - \frac{\partial R}{\partial \xi_1} \frac{\partial Z}{\partial \xi_2} \right) d\boldsymbol{\xi}_1 d\boldsymbol{\xi}_2, \tag{28e}$$

$$Q_{1,2}^{\alpha,\beta} = -2\pi \left(\eta_2 R \mathbf{A}_\Phi + \eta_3 \frac{m\rho_L}{Z} R b_\Phi \right)_{\xi_1=\xi_1^\alpha, \xi_2=\xi_2^\beta}, \tag{28f}$$

$$Q_{1,3}^{\alpha,\beta} = -\int_{\xi_2^0}^{\xi_2^1} \left[\left(\eta_2 \mathbf{A}_R + \eta_3 \frac{m v_\| \rho_L}{Z} \mathbf{b}_R \right) \frac{\partial R}{\partial \xi_2} + \left(\eta_2 \mathbf{A}_Z + \eta_3 \frac{m v_\| \rho_L}{Z} \mathbf{b}_Z \right) \frac{\partial Z}{\partial \xi_2} \right]_{\xi_1=\xi_1^\alpha} d\xi_2, \tag{28g}$$

$$Q_{2,3}^{\alpha,\beta} = -\int_{\xi_2^0}^{\xi_2^1} \left[\left(\eta_2 \mathbf{A}_R + \eta_3 \frac{m v_\| \rho_L}{Z} \mathbf{b}_R \right) \frac{\partial R}{\partial \xi_1} + \left(\eta_2 \mathbf{A}_Z + \eta_3 \frac{m v_\| \rho_L}{Z} \mathbf{b}_Z \right) \frac{\partial Z}{\partial \xi_1} \right]_{\xi_2=\xi_2^\alpha} d\xi_1, \tag{28h}$$

$$Q_{d',d}^{\alpha,\beta} = -Q_{d,d'}^{\alpha,\beta} \tag{28i}$$

and $\eta_0^\alpha = v_\|(\xi_0^\alpha)$, $\eta_1^\alpha = v_\|(\xi_0^\alpha)\mu$, $\eta_2 = (v_\|^2(\xi_0^1) - v_\|^2(\xi_0^0))/2$ and $\eta_3 = (v_\|^3(\xi_0^1) - v_\|^3(\xi_0^0))/3$. Noting that the quantities $Q_{d,3}^{\alpha,\beta}$ are independent of β for all d, we have from (23) that

$$\int_{\mathbf{X}(V_0^\alpha)} \boldsymbol{\sigma} = \sum_{d'\neq 0} \sum_{\beta=0,1} (-1)^{d'+1+\beta} Q_{0,d'}^{\alpha,\beta} = \sum_{\beta=0,1} (-1)^\beta \left(Q_{0,1}^{\alpha,\beta} - Q_{0,2}^{\alpha,\beta} \right), \tag{29a}$$

$$\int_{\mathbf{X}(V_1^\alpha)} \boldsymbol{\sigma} = \sum_{d'\neq 1} \sum_{\beta=0,1} (-1)^{d'+1+\beta} Q_{1,d'}^{\alpha,\beta} = \sum_{\beta=0,1} (-1)^\beta \left(Q_{0,1}^{\alpha,\beta} - Q_{1,2}^{\alpha,\beta} \right), \tag{29b}$$

$$\int_{\mathbf{X}(V_2^\alpha)} \boldsymbol{\sigma} = \sum_{d'\neq 2} \sum_{\beta=0,1} (-1)^{d'+1+\beta} Q_{2,d'}^{\alpha,\beta} = \sum_{\beta=0,1} (-1)^\beta \left(Q_{0,2}^{\alpha,\beta} - Q_{1,2}^{\alpha,\beta} \right), \tag{29c}$$

$$\int_{\mathbf{X}(V_3^\alpha)} \boldsymbol{\sigma} = \sum_{d'\neq 3} \sum_{\beta=0,1} (-1)^{d'+1+\beta} Q_{3,d'}^{\alpha,\beta} = 0, \tag{29d}$$

which, together with (18), yields

$$\int_{\mathbf{X}(W)} \nabla_{\mathbf{X}} \cdot \widetilde{\mathbf{u}} \, d\mathbf{x} = \sum_{d=0}^{3} \sum_{\alpha=0,1} (-1)^{1+\alpha+d} \int_{\mathbf{X}(V_d^\alpha)} \boldsymbol{\sigma} = 0. \tag{30}$$

Trivially,

$$\int_{\mathbf{X}(W)} \nabla_{\mathbf{X}} \cdot \widehat{\mathbf{u}} \, d\mathbf{x} = \sum_{\alpha=0,1} (-1)^{1+\alpha} \int_{V_0^\alpha} N_{0,0} \widehat{\mathbf{u}}_0 d\mathbf{V}_{\boldsymbol{\xi}} = 0, \tag{31}$$

and therefore $\mathbf{u}$ is discretely divergence free.

The assumption of axisymmetric fields allows additional simplifications of the quantities $Q_{0,1}$, $Q_{0,2}$, and $Q_{1,2}$. Assuming that $\mathbf{E}$ has no toroidal component, we observe that

$$-(\mathbf{b} \times \mathbf{E})_Z \frac{\partial R}{\partial \xi_2} + (\mathbf{b} \times \mathbf{E})_R \frac{\partial Z}{\partial \xi_2} = -b_\Phi \left(\frac{\partial \phi}{\partial R} \frac{\partial R}{\partial \xi_2} + \frac{\partial \phi}{\partial Z} \frac{\partial Z}{\partial \xi_2} \right) = -\frac{B_\Phi}{B} \frac{\partial \phi}{\partial \xi_2}, \tag{32}$$

and similarly, since ∇B has no toroidal component,

$$(\mathbf{b} \times \nabla B)_Z \frac{\partial R}{\partial \xi_2} - (\mathbf{b} \times \nabla B)_R \frac{\partial Z}{\partial \xi_2} = -\frac{B_\Phi}{B} \frac{\partial B}{\partial \xi_2} = -B_\Phi \frac{\partial \ln(B)}{\partial \xi_2}. \tag{33}$$

Hence, since $RB_\Phi = (RB)_{\text{tor}}$ is a constant [23],

$$Q_{0,1}^{\alpha,\beta} = -2\pi \rho_L (RB)_{\text{tor}} \left[\eta_0^\alpha \int_{\xi_2^0}^{\xi_2^1} \left(\frac{1}{B} \frac{\partial \phi}{\partial \xi_2} \right)_{\xi_1=\xi_1^\beta} d\xi_2 + \frac{\eta_1^\alpha}{2Z} \ln \frac{B(\xi_1^\beta, \xi_2^1)}{B(\xi_1^\beta, \xi_2^0))} \right]. \tag{34}$$

Similarly,

$$Q_{0,2}^{\alpha,\beta} = -2\pi\rho_L(RB)_{\text{tor}}\left[\eta_0^\alpha\int_{\xi_1^0}^{\xi_1^1}\left(\frac{1}{B}\frac{\partial\phi}{\partial\xi_1}\right)_{\xi_2=\xi_2^\beta}d\xi_1 + \frac{\eta_1^\alpha}{2Z}\ln\frac{B(\xi_1^1,\xi_2^\beta)}{B(\xi_1^0,\xi_2^\beta)}\right]. \tag{35}$$

Letting Ψ denote the magnetic flux, we may take $\mathbf{A}_\Phi = \Psi/R$, yielding

$$Q_{1,2}^{\alpha,\beta} = -2\pi\left(\eta_2\Psi + \eta_3\frac{m\rho_L}{Z}\frac{(RB)_{\text{tor}}}{B}\right)_{\xi_1=\xi_1^\alpha,\xi_2=\xi_2^\beta}. \tag{36}$$

Summarizing the above, the face integrals of the mapped normal velocities are

$$\int_{V_0^\alpha}(\mathbf{N}^T\mathbf{u})_0 d\mathbf{V}_{\boldsymbol{\xi}} = \sum_{\beta=0,1}(-1)^\beta\left(Q_{0,2}^{\alpha,\beta} - Q_{0,1}^{\alpha,\beta}\right) + \widehat{U}^\alpha \tag{37a}$$

$$\int_{V_1^\alpha}(\mathbf{N}^T\mathbf{u})_1 d\mathbf{V}_{\boldsymbol{\xi}} = \sum_{\beta=0,1}(-1)^\beta\left(Q_{0,1}^{\alpha,\beta} - Q_{1,2}^{\alpha,\beta}\right), \tag{37b}$$

$$\int_{V_2^\alpha}(\mathbf{N}^T\mathbf{u})_2 d\mathbf{V}_{\boldsymbol{\xi}} = \sum_{\beta=0,1}(-1)^\beta\left(Q_{1,2}^{\alpha,\beta} - Q_{0,2}^{\alpha,\beta}\right), \tag{37c}$$

$$\int_{V_3^\alpha}(\mathbf{N}^T\mathbf{u})_3 d\mathbf{V}_{\boldsymbol{\xi}} = 0, \tag{37d}$$

where $Q_{0,1}$, $Q_{0,2}$, and $Q_{1,2}$ are defined by (34), (35) and (36), respectively, and

$$\widehat{U}^\alpha = \frac{2\pi}{m}\int_{\xi_1^0}^{\xi_1^1}\int_{\xi_2^0}^{\xi_2^1}\mathbf{B}\cdot\left(Z\mathbf{E} - \frac{\mu}{2}\nabla B\right)\left(\frac{\partial R}{\partial\xi_1}\frac{\partial Z}{\partial\xi_2} - \frac{\partial R}{\partial\xi_2}\frac{\partial Z}{\partial\xi_1}\right)Rd\xi_1 d\xi_2. \tag{38}$$

We note that no metric factors appear in $Q_{0,1}$, $Q_{0,2}$, and $Q_{1,2}$, which are computed exactly from the evaluation of magnetic field data at configuration space cell vertices, except for the cell face integrals of the transverse ϕ derivatives divided by B. These latter integrals can be computed using the fourth-order product formula (7), in which the resulting ϕ integrals can be evaluated exactly in terms of nodal ϕ values. This fact plays a critical role in avoiding a severe instability that can arise in the high-order, finite-volume modeling of drift waves [11].

By tracing the individual terms of the gyrokinetic velocity (2) through the above development, the physical meaning of the terms in (34), (35), (36) and (38) can be identified. The $\mathbf{B}\cdot\mathbf{E}$ and $\mathbf{B}\cdot\nabla B$ acceleration terms in (38) are clear. The first and second terms in (34) and (35) are the $\mathbf{E}\times\mathbf{B}$ and ∇B drifts, respectively. The second term in (36) is the curvature drift. The first term in (36) is the parallel streaming contribution, whose magnitude, as mentioned in Section 2, dominates those of the drift terms by a few orders of magnitude for typical tokamak parameters. In addition to the fact that the parallel streaming, ∇B drift and curvature drift terms are all computed exactly, an important consequence of the velocity discretization described here is that, on radial cell faces V_1^α contained in a flux surface, parallel streaming makes zero (to machine precision) contribution to the normal velocity component (37b), due to the subtraction of the uniform Ψ values effected by the β sum. This fact ensures that parallel velocity discretization error cannot dominate the drift terms, thereby masking the contribution of the latter via what is sometimes referred to as "numerical pollution" [44].

3.3. Multiblock extension

The single block discretization just described can be extended to the multiblock edge plasma geometry (Fig. 3). In order to apply at block interfaces the same fourth-order reconstruction (13) used in the block interiors, a halo of "extrablock" ghost cells is filled by interpolation from surrounding cell-averaged data. Assuming that the smooth mappings on each block possess smooth extensions beyond their respective boundaries (as discussed later in Section 4), these extrablock ghost cells are generated by simply applying the mapping to an extended computational grid. Fig. 4 shows an example of filling an extrablock ghost cell near the X point. The only aspect the calculation of fluxes at interblock boundaries that is special is a post-processing step performed to restore strict conservation. Since there is no guarantee that the fluxes calculated on each side of a multiblock interface using the above procedure will agree to better than fourth order, the two fluxes are averaged to define a consistent value for use on both adjacent blocks. The key element is therefore the interpolation of valid neighbor block data to extrablock ghost cells. The approach we employ here is independent of the edge plasma application and is described in detail in [38].
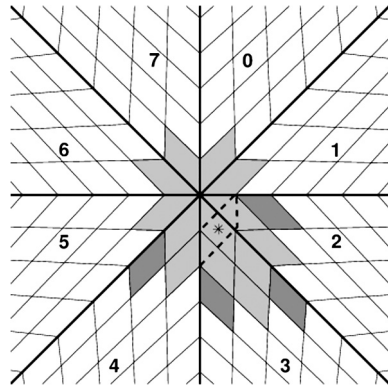
Fig. 4. Multiblock interpolation near the X point. The asterisk * indicates the center of an extrablock ghost cell of block number 4, which is filled by interpolation from the data in the shaded cells of neighboring blocks. The shading distinguishes a technical detail that is fully described in [38].

4. Mapping the edge geometry

The use of mapped coordinates to accommodate strong anisotropy along magnetic field lines requires the construction of block mappings from computational to physical coordinates in which one of the computational coordinates parameterizes flux surfaces. In this section, we describe an approach based on the assumed availability of the magnetic flux $\Psi = \Psi(R, Z)$ in cylindrical coordinates, from which the (assumed axisymmetric) magnetic field $\mathbf{B} = (B_R, B_\Phi, B_Z)$ is obtained as

$$B_R(R, Z) = -\frac{1}{R}\frac{\partial \Psi(R, Z)}{\partial Z}, \quad B_\Phi(R, Z) = \frac{(RB)_{\text{tor}}}{R}, \quad B_Z(R, Z) = \frac{1}{R}\frac{\partial \Psi(R, Z)}{\partial R}, \tag{39}$$

where $(RB)_{\text{tor}}$ is a constant.[3] This provides a smooth representation of the magnetic field for use in the construction of mappings as well as the evaluation of the gyrokinetic velocity (2). The magnetic flux may be obtained, for example, as the result of a separate equilibrium calculation or a spectral interpolation of experimental flux measurements.

Although field lines define smooth curves in three-dimensional space, for axisymmetric edge geometries the use of fully flux-aligned coordinate mappings is problematic near the X point. As shown in Fig. 5, flux surfaces become increasingly "kinked" approaching the X point, resulting in diverging metric factors for flux-aligned coordinate mappings. As noted at the end of Section 3.2, no metric factors appear in the normal velocity integrals (37a), so the singularity of flux-aligned metrics does not affect their calculation. On the other hand, reconstruction of the distribution function on block interfaces using the interpolation described in Section 3.3 requires not only smooth mappings up to block boundaries, but also some distance beyond to accommodate the ghost cell halo. We therefore relax the assumption of flux-aligned mappings near the X point. Although the cost of such a modification is likely the need for increased resolution, this is mitigated by the fact that, since the poloidal component of the magnetic field is small near the X point, anisotropy is less of a concern there and thus the need for strict flux alignment is reduced.

The poloidal grid lines of a dealigned grid can be constructed as the level surfaces of a modified flux function Ψ obtained by the blending of the original magnetic flux function Ψ_0, given in the vicinity of the X point by

$$\Psi_0 - \Psi_X \approx \widetilde{R}^2 - \widetilde{Z}^2, \tag{40}$$

and the block-aligned linear function

$$\Psi_{\text{lin}} = D\left(|\widetilde{R}| - |\widetilde{Z}|\right), \tag{41}$$

such that outside a transition radial distance D, the blended flux becomes the original flux, whereas inside the flux is given by the block-aligned flux. Here, Ψ_X is the value of Ψ_0 at the X point (R_X, Z_X) and $(\widetilde{R}, \widetilde{Z})$ are the linear coordinate transforms of (R, Z). We define the blended flux function by

$$\Psi = \Psi_X + \tanh\left(\frac{r}{D}\right)(\Psi_0 - \Psi_X) + \alpha\left(1 - \tanh\left(\frac{r}{D}\right)\right)\Psi_{\text{lin}}, \tag{42}$$

where $r = (\widetilde{R}^2 + \widetilde{Z}^2)^{1/2}$, and α is an optimization parameter of the order unity.

---

[3] In general, $(RB)_{\text{tor}}$ is a function of Ψ, but is constant under the common assumption of negligible poloidal plasma current density relative to that of the toroidal field coils [23].
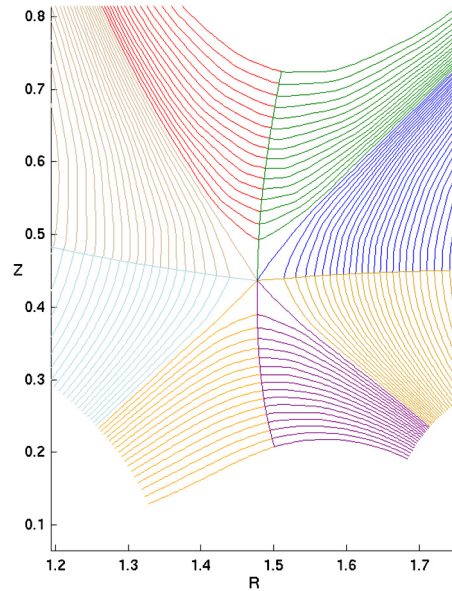
Fig. 5. Flux surfaces in the vicinity of the X point become increasingly kinked, precluding the introduction of a smooth flux-aligned coordinate system in this area.

The linear coordinate transforms $(\widetilde{R}, \widetilde{Z})$ are related to the (R, Z) coordinate system by

$$\widetilde{R} = a_1(R - R_X) + b_1(Z - Z_X), \tag{43a}$$

$$\widetilde{Z} = a_2(R - R_X) + b_2(Z - Z_X), \tag{43b}$$

where the linear coefficients can be found by solving a system of nonlinear algebraic equations. Introducing the original flux function expansion near the X point as

$$\Psi_0 - \Psi_X = a(R - R_X)^2 + b(R - R_X)(Z - Z_X) + c(Z - Z_X)^2 \tag{44}$$

and making use of (40), we obtain

$$\begin{aligned} a_1^2 - a_2^2 &= a, \\ b_1^2 - b_2^2 &= c, \\ 2a_1 b_1 - 2a_2 b_2 &= b, \\ a_1 a_2 + b_1 b_2 &= 0, \end{aligned} \tag{45a}$$

where the last equation in (45a) is the orthogonality condition of the $(\widetilde{R}, \widetilde{Z})$ coordinate system. Because the quadratic form (44) for a magnetic flux near the X point is hyperbolic, $b^2 - 4ac > 0$, which implies that $b^2 + 2c(-a\sqrt{b^2 + (a-c)^2} + c) > 0$ if $b \neq 0$ (see Appendix A.5). Letting $\delta = \sqrt{b^2 + (a-c)^2}$, the solution of the system (45a) is then

$$a_1 = -\frac{(a + \delta - c)\sqrt{b^2 + 2c(-a + \delta + c)}}{2b\delta^{1/2}}, \tag{46a}$$

$$a_2 = -\frac{\sqrt{2a^2 + b^2 - 2a(\delta + c)}}{2\delta^{1/2}}, \tag{46b}$$

$$b_1 = -\frac{\sqrt{b^2 + 2c(-a + \delta + c)}}{2\delta^{1/2}}, \tag{46c}$$

$$b_2 = -\frac{(a + \delta - c)\sqrt{2a^2 + b^2 - 2a(\delta + c)}}{2b\delta^{1/2}}. \tag{46d}$$

Solutions for the special case of $b = 0$ can be obtained by applying L'Hospital's rule to the above expressions.

Given the hybrid flux (42) just constructed, the desired poloidal grid lines correspond to level surfaces of Ψ spaced equidistantly in Ψ and are obtained by ray tracing. The radial grid lines are obtained as follows:

1. Construct an arc length mapping $(R(\ell_\theta), Z(\ell_\theta))$ along the (modified) separatrix;
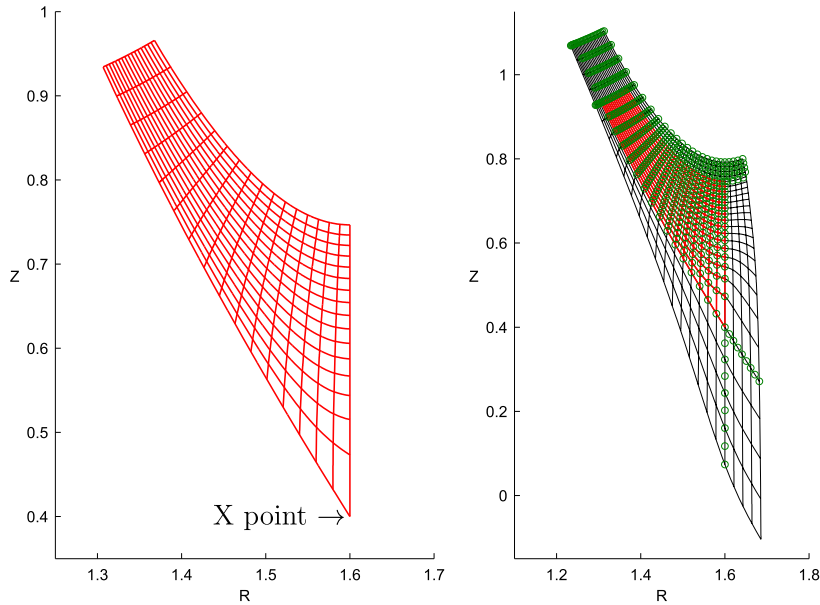
Fig. 6. Construction of the LCORE mapping grid. Left: A grid is generated that is flux-dealigned near the X point, boundary-aligned near the right-hand boundary and locally-orthogonal away from the X point. Right: Ghost cells are added by evaluating RBF interpolants of the (R, Z) coordinates of the points indicated by the circles, comprised of the union of the valid block grid (red) points, physical boundary points and points along the extended block boundaries. (For interpretation of the colors in the figure(s), the reader is referred to the web version of this article.)

2. Position grid nodes on the separatrix such that they are equidistant in ℓ_θ; then
3. From those points, ray trace radial grid lines as follows. In the MCORE and MCSOL blocks, trace the radial grid lines normal to Ψ, yielding a locally orthogonal grid in those blocks. In the remaining blocks, trace the radial grid lines parallel in directions given by a smooth blending of the normal-to-Ψ and block boundary directions. The purpose of this blending is to ensure that (i) the grid is locally orthogonal in a neighborhood of such radial block boundaries and (ii), in a neighborhood of the radial block boundaries that do contain the X point, the radial grid lines are nearly parallel to those boundaries. The purpose of goal (i) is to enable the construction of a global MMB grid in which ghost cells overlap the valid cells of neighboring blocks at the poloidal interface between MCORE and LCORE or RCORE, as well as between MCSOL and LCSOL or RCSOL, so that ghost cell data can be obtained by direct copying rather than interpolation. Goal (ii) avoids the generation of small cells that can result in an unnecessary stability limitation for explicit time integration, as well as the possibility of large derivatives in the metric factors computed from the resulting mapping.

Fig. 6 (left) shows the result of applying the above procedure in the LCORE block of the magnetic equilibrium used in the numerical tests performed in Section 6. To add ghost cells, the block boundaries of the dealigned block grid are first extended in each direction the desired number M of ghost cells. In the LCORE example shown on the right-hand side of Fig. 6, $M = 4$ points (indicated by circles) have been added along each boundary extension. These points (32 in the Fig. 6 example) are combined with the block grid points and a layer of M points along the two block boundaries not containing the X point (which are obtainable from the magnetic flux in the same manner as the aligned interior points) to obtain a set of points $\{(R(\xi_i, \eta_i), Z(\xi_i, \eta_i)) : 1 \leq i \leq N\}$ representing N evaluations of a mapping $(\xi, \eta) \rightarrow (R(\xi, \eta), Z(\xi, \eta))$ from logical to physical coordinates. We obtain the desired mapping as the radial basis function (RBF) interpolants

$$R(\xi, \eta) = \sum_{i=1}^{N} \alpha_{R,i} [(\xi - \xi_i)^2 + (\eta - \eta_i)^2]^{3/2}, \tag{47a}$$

$$Z(\xi, \eta) = \sum_{i=1}^{N} \alpha_{Z,i} [(\xi - \xi_i)^2 + (\eta - \eta_i)^2]^{3/2}, \tag{47b}$$

by solving linear systems for the coefficients $(\alpha_{R,i}, \alpha_{Z,i})$ such that (47) interpolates the points $(R(\xi_i, \eta_i), Z(\xi_i, \eta_i)), 1 \leq i \leq N$. The remaining ghost cell vertex coordinates are then obtained by evaluating (47) at the corresponding logical indices, yielding the full ghost cell region, as indicated by the black grid in the right-hand side of Fig. 6.

Since the MCORE and MCSOL blocks do not contain the X point, flux-aligned locally orthogonal grids in these blocks can be generated by simple ray tracing. Because the grid dealignment in the blocks that do contain the X point is limited
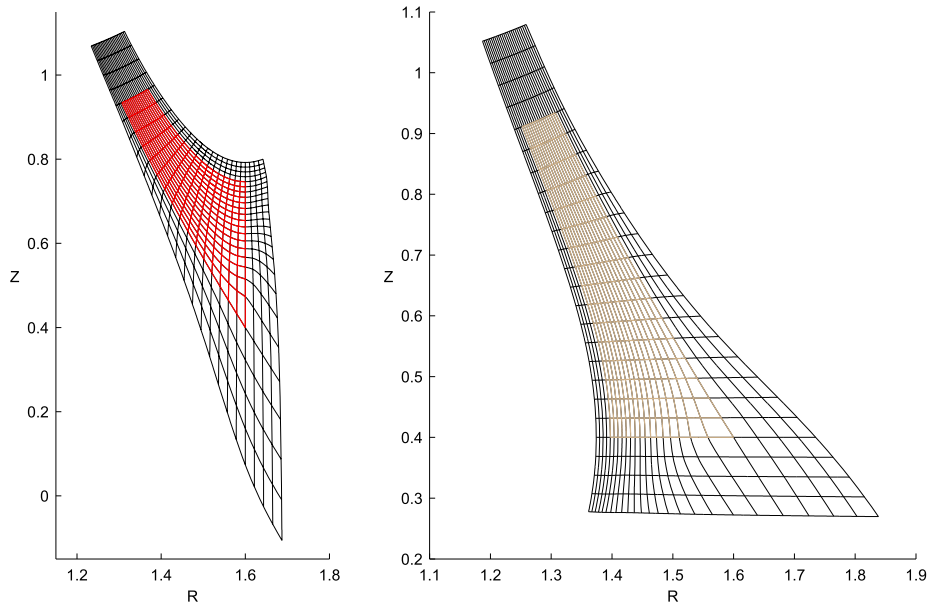
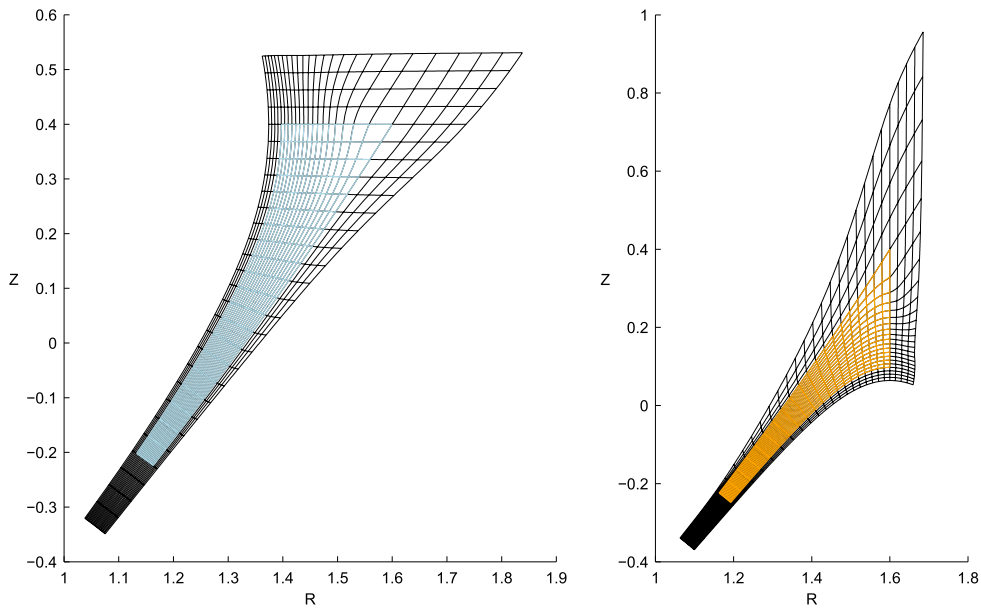**Fig. 7.** LCORE (left) and LCSOL (right) mapping grids.

Fig. 8. LSOL (left) and LPF (right) mapping grids.

to a region that is bounded away from the MCORE and MCSOL block boundaries due to the ray tracing of radial grid lines (see Section 4), ghost cells at all intrablock boundaries involving MCORE and MCSOL can be obtained from valid cells in adjacent blocks. For ghost cells constructed in this manner, the filling of the ghost cell halo described in Subsection 3.3 can be performed by direct copying of valid data rather than interpolation.

Figs. 7 through 9 show the extended block grids generated by the above approach for the LCORE, LCSOL, LSOL, LPF, MCORE and MCSOL blocks of the Section 6 example, coarsened by a factor of two for better plotting visibility. The RCORE, RCSOL, RSOL and RPF blocks are symmetric with their left-hand side counterparts. The black grid lines demarcate the extended ghost cells.

The purpose of the grid generation just described is to enable the discrete representation of the block mappings required by the mapped multiblock discretization described in Section 3. Using the extended block grids (*e.g.*, Figs. 7 through 9), we construct sixth-order B-spline interpolants of the (R, Z) physical coordinate components, which yields mappings with four continuous derivatives. The spatial grid used to discretized the Vlasov system is then the image under this mapping of a
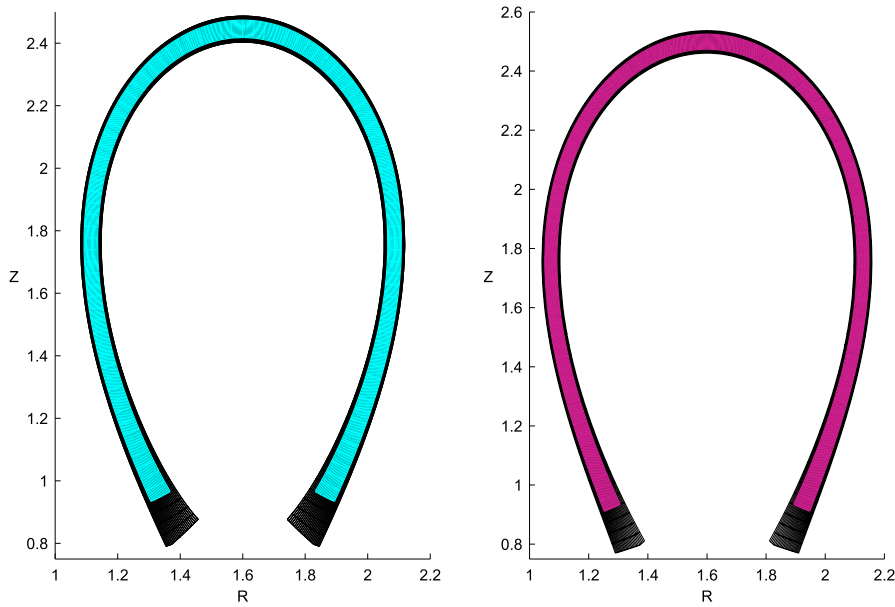
Fig. 9. MCORE (left) and MCSOL (right) mapping grids.

computational grid at the desired resolution, which in general will not be the same as the block grids used to define the mapping. The grid generation performed to define the mapping is only performed once for a given magnetic flux. A few additional points are in order concerning this approach:

1. The RBFs used in (47) are also known as polyharmonic smoothing splines [3]. In addition to being smooth, such functions minimize a particular functional of higher derivatives, which makes them a robust choice for the high-order extrapolation being performed here.
2. The RBF interpolants (47) might also appear to provide a convenient mapping choice, having already constructed them for the purpose of generating ghost cells. Unfortunately, since each such block interpolant is defined using data specific to its own block, there is no guarantee that the interpolants will be continuous along interblock boundaries (*i.e.*, *between* common grid points where they do in fact agree), which is required by our mapped discretization approach. In contrast, due to their tensor product definition, the B-spline interpolants are uniquely defined by their values at the shared points along interblock boundaries and are therefore continuous across such boundaries.
3. Although the vertices of the block grids used to define the block mappings are flux-aligned by construction, except in the dealignment neighborhood of the X point, the vertices of grids obtained by evaluating the B-spline interpolants are not guaranteed to be similarly flux-aligned. It is therefore important to employ an adequate number of poloidal points in the block mapping grids to reduce the error due to grid dealignment. In studies we have performed to date, we find that using 128 or 256 poloidal cells in the core region of the mapping grid is likely sufficient for realistic edge geometries. If dealignment error is an acute concern for some reason, one always has the option of employing a grid consistent with that used to construct the mapping so that no interpolation is performed.

5. COGENT

The spatial discretization approach described above provides the foundation of the COGENT (COntinuum Gyrokinetic Edge New Technology) code [10,12,14,15,17], which we have been developing for the solution of gyrokinetic systems in mapped multiblock geometries, including those describing the tokamak edge. Although this paper is addressing just the Vlasov operator discretization, we include this short description of the more general code environment in which it is being used.

To obtain self-consistent electric fields, COGENT includes an electrostatic model. The potential Φ depends upon the charge density of the species distribution functions f_α being evolved by (1)–(3), where α is a species index, which in turn depend upon Φ in the velocity calculation. Because the f_α are computed in gyrocenter coordinates and the Poisson equation is posed in the lab frame, the velocity integral yielding the ion charge density must therefore be split into two pieces. In the long wavelength limit $k_\perp \rho \ll 1$, where $k_\perp$ is the magnetic field perpendicular wave number and ρ is the ion gyroradius, the gyrokinetic Poisson equation is

$$\nabla_{\mathbf{X}} \cdot \left\{ \left[\lambda_D^2 \mathbf{I} + \rho_L^2 \sum_\alpha \frac{Z_\alpha \bar{n}_\alpha}{m_\alpha \Omega_\alpha^2} \left(\mathbf{I} - \mathbf{b}\mathbf{b}^T \right) \right] \nabla_{\mathbf{X}} \Phi \right\} = n_e - \sum_\alpha Z_\alpha \bar{n}_\alpha, \tag{48}$$

where $\nabla_{\mathbf{X}}$ denotes the gradient with respect to the normalized lab frame coordinate and λ_D is the normalized Debye length. At shorter wavelengths, $k_\perp \rho \approx 1$, (48) must be augmented by terms involving the gyroaveraging of distribution functions [22], which is a planned addition to COGENT. The quantity

$$\bar{n}_\alpha(x,t) = \frac{1}{m_\alpha} \int f_\alpha(x, v_\parallel, \mu, t) B_\parallel^*(x, v_\parallel) dv_\parallel d\mu \tag{49}$$

is the ion gyrocenter density, which is the gyrophase-independent part of the integration of the gyrocenter distribution function f_α over velocity. The second term in the left-hand side of (48) is the polarization density, which is the gyrophase-dependent part of the velocity integration of f_α. Since this piece depends upon the potential, we must combine it with the usual Laplacian (the first term in (48)) in the construction of the linear operator to be solved for Φ. Here, $\mathbf{b}$ denotes the unit vector in the direction of the magnetic field, Z_α is the charge state, m_α is the mass, and Ω_α is the gyrofrequency. We note that for typical tokamak parameters, $\lambda_D \ll \rho_L$, and hence the polarization density term dominates. Because the electron gyroradius is small, a similar splitting of the electron density is omitted.

COGENT includes a range of collision operators, which are included in the right-hand side of (1). These include a Krook model, a drag-diffusion operator in parallel velocity space, Lorentz collisions, a linearized Fokker–Planck model conserving momentum and energy [12], and a fully nonlinear Fokker–Planck model of Coulomb collisions [13]. Since the latter are convection–diffusion operators in velocity space, they also require appropriate discretizations, which have been compatibly developed using the same high-order, finite-volume formalism underlying the Vlasov term treatment described herein [18, 19].

Time integration in COGENT is performed using either an explicit fourth-order Runge Kutta (RK4) method or a semi-implicit additive Runge–Kutta (ARK) time integration scheme, via second-order (three-stage) [20], third-order (four-stage) [32], or fourth-order (six-stage) [32] options. The ARK approach is used to treat fast collisional time scales and/or electron dynamics. In both methods, evaluation of the discrete Vlasov operator as described herein is performed as a function evaluation, where the gyrokinetic Poisson equation (48) is solved at each stage using the predicted distribution functions, yielding the self-consistent electric field needed to compute the phase space velocity (2). In the ARK approach, a Jacobian-free Newton–Krylov method is used to solve the nonlinear equations that arise in the implicit updates [19].

COGENT is built upon the Chombo structured adaptive mesh refinement (AMR) framework [9]. Although COGENT does not currently utilize Chombo's AMR capabilities, Chombo provides many data structures and parallel operations that are well-suited for mapped multiblock algorithms, including data containers for mesh-dependent quantities distributed over processors and support for the mapped grid formalism described in Section 3. Multidimensional data types and operations, such as the computation of two-dimensional densities from four-dimensional distribution functions and the ability to independently decompose configuration and phase space, are also provided.

6. Truncation error verification

In this section, we demonstrate the high-order convergence of the strategy described in the preceding sections when applied to the spatial discretization of (1)–(3) in an edge geometry. Using (39), the magnetic field $\mathbf{B}$ is defined in terms of an analytically prescribed poloidal flux Ψ developed in [15] and reproduced here, which results in a magnetic geometry that is roughly characteristic of the DIII-D tokamak. Although our approach only requires a smooth flux representation, including one obtained by interpolation from experimental data, we consider an analytic model here to avoid any additional complications from noise or other observational errors. Specifically, we begin by considering a normalized poloidal flux function

$$\Psi_N(R, Z) = \cos[c_1(R - R_0)/L_N] + c_2 \sin[(Z - Z_0)/L_N] - c_3(Z - Z_0)/L_N, \tag{50}$$

where R and Z are the radial (distance from the magnetic axis) and vertical (parallel to the magnetic axis) coordinates (in meters), respectively; $Z_X = -L_N \arccos(c_3/c_2)$ corresponds to the vertical position of the X point; $c_1 = 1.2$, $c_2 = 0.9$, and $c_3 = 0.7$ are the dimensionless constant shape factors; $L_N = 1$ m is a normalizing spatial scale; $R_0 = 1.6$ m is the major radius coordinate corresponding to the location of the magnetic axis; and $Z_0 = 0.4 + L_N \arccos(c_3/c_2)$ is a constant vertical shift (in meters) adopted for visualization purposes. For the simulations reported, the radial width of the open and closed field line regions is taken to be $\Delta_R = 6.7$ cm as measured at the top of the tokamak. The poloidal flux (in Webers) is then defined as

$$\Psi = \Psi_N \bar{B}_\theta R_{\text{mp}} \left[\left(\frac{\partial \Psi_N}{\partial R} \right)^2 + \left(\frac{\partial \Psi_N}{\partial Z} \right)^2 \right]_{(R_{\text{mp}}, Z_{\text{mp}})}^{-1/2}, \tag{51}$$

where, $\bar{B}_\theta = 0.16$ T is the magnitude of the poloidal magnetic field at the intersection of the separatrix and the outboard midplane corresponding to $R_{\text{mp}} = 2.11$ m and $Z_{\text{mp}} = Z_0 + L_N \arccos(c_3/c_2) = 1.76$ m, and the directions of the coordinate

Table 1
Grid sizes for the convergence study.

Grid m	MCORE MCSOL	Blocks containing the X point	$v_\parallel$	μ	Number of cells
1	8×48	8×8	24	24	737,280
2	16×96	16×16	48	48	11,796,480
3	32×192	32×32	96	96	188,743,680
4	64×384	64×64	192	192	3,019,898,880

system unit vectors are such that $\mathbf{e}_R \times \mathbf{e}_\phi = \mathbf{e}_Z$. The toroidal field component is defined by setting $(RB)_{\text{tor}} = 3.5$ T-m. Using Ψ, the grid generation procedure described in Section 4 yields the mapping blocks displayed in Figs. 7 through 9.

Next, we define $\psi(R, Z) = (\Psi(R, Z) - \Psi_A)/(\Psi_S - \Psi_A)$, where Ψ_A and Ψ_S are the on-axis and separatrix values of Ψ, respectively. In terms of this normalized flux, we let

$$f(R, Z, v_\parallel, \mu) = \frac{n(R, Z)}{\pi^{1/2}(2T/m)^{3/2}} \exp\left[\frac{-(mv_\parallel^2 + \mu B(R, Z))}{2T} \right] \tag{52}$$

be a Maxwellian distribution function with density

$$n(R, Z) = \tanh\left[25(0.9 - \psi(R, Z))\right] + 1.1, \tag{53}$$

temperature $T = 1$ and mass $m = 1$. Also let

$$\phi(R, Z) = -\frac{T}{Z}\ln(n(R, Z)). \tag{54}$$

Except for R and Z, which only enter through the dimensional Ψ and B defined earlier, all other quantities incorporate the normalizations described in Appendix A.1, with the Table 2 reference parameters $\tilde{n} = 10^{20}$ m^{-3}, $\tilde{T} = 1$ keV, $\tilde{L} = 1$ m, $\tilde{m} = 1$ u, $\tilde{B} = 1$ T. As shown in Appendix A.6, the Vlasov operator in (1)–(3) with the electric field computed from (54) vanishes when applied to the Boltzmann equilibrium distribution function (52). The application of the discretized operator therefore represents the truncation error of the mapped multiblock spatial discretization approach, which we can measure directly. In obtaining the results reported below, we employ the fourth-order, centered-difference formula (13) with WENO-like limiter modifications described in [25].

We consider the four-grid sequence specified in Table 1, obtained by refining each phase space dimension by a factor of two relative to an initial grid. We are interested in the behavior of the truncation error at locations where the error is likely to be greatest, rather than some globally integrated measure. We therefore inspect the error at block corners and boundaries, both physical and intrablock, as well as a few points in the interior of blocks to quantify the performance of the interior scheme there as well. Since the phase space geometry is multiblock only in the configuration space coordinates, we also want to ensure that the error is not dominated by the velocity space discretization, and thus possibly masking error due to the multiblock treatment of configuration space. We therefore truncate the velocity space domain to $-1 \leq v_\parallel \leq 1$ and $0 \leq \mu \leq 2$, relative to the thermal velocity scaling described in Appendix A.1, which avoids the need for even finer velocity space grids than those shown in Table 1, which we have verified are sufficient to achieve adequate resolution.

We specify a set S of cells (i, j), indicated in Fig. 10, relative to the coarsest ($m = 1$) grid in Table 1. We consider only the LCORE and MCORE blocks, with LCORE representing one of the eight blocks containing the X point and MCORE representing one of the two blocks that do not. Further, we consider only the left side of MCORE due to symmetry. As can be seen in Fig. 10, cells 0, 9 and 12 lie completely within block interiors, cells 1 through 4, 10, 11, 13 and 14 lie on block boundary interiors, and cells 5 though 8, 16 and 17 lie at cell corners. Of the cells at block boundaries, cells 1, 5, 7, 10, 14 and 16 also lie at physical boundaries. Cell 8 is adjacent to the X point. For each (i, j) in S, we compute the velocity space volume-weighted sums

$$\tau_{i,j}^{(1)} = \frac{\sum_{k,\ell} \left| r_{i,j,k,\ell}^{(1)} \right| V_{i,j,k,\ell}^{(1)}}{\sum_{k,\ell} V_{i,j,k,\ell}^{(1)}}, \tag{55}$$

where $r_{i,j,k,\ell}^{(1)}$ is the discrete cell average on phase space cell (i, j, k, ℓ) of the Vlasov operator applied to the Boltzmann equilibrium solution and $V_{i,j,k,\ell}^{(1)}$ is the cell volume. For each (i, j) in S, let $I_{i,j}^{(m)}$ denote the set of configuration space indices comprised of cells contained in the refinement of cell (i, j) in grid m for $2 \leq m \leq 4$. Letting $V_{i,j,k,\ell}^{(m)}$ again denote the phase space volumes on the respective grids, define

$$\tau_{i,j}^{(m)} = \frac{\sum_{(i',j') \in I_{i,j}^{(m)}} \sum_{k,\ell} \left| r_{i',j',k,\ell}^{(m)} \right| V_{i',j',k,\ell}^{(m)}}{\sum_{(i',j') \in I_{i,j}^{(m)}} \sum_{k,\ell} V_{i',j',k,\ell}^{(m)}}, \quad 2 \leq m \leq 4, \tag{56}$$

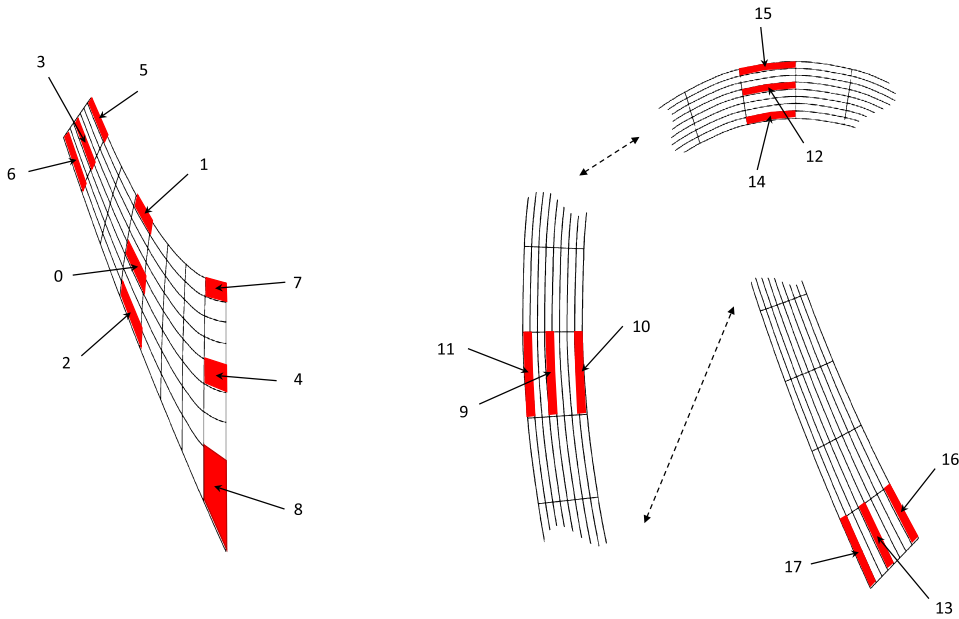which correspond to grid refined evaluations of (55).

Fig. 10. Test index locations in LCORE (left) and MCORE (right). Cells 0, 9 and 12 lie completely within block interiors, cells 1 through 4, 10, 11, 13 and 14 lie on block boundary interiors, and cells 5 though 8, 16 and 17 lie at cell corners. Of the cells at block boundaries, cells 1, 5, 7, 10, 14 and 16 also lie at physical boundaries. Cell 8 is adjacent to the X point.
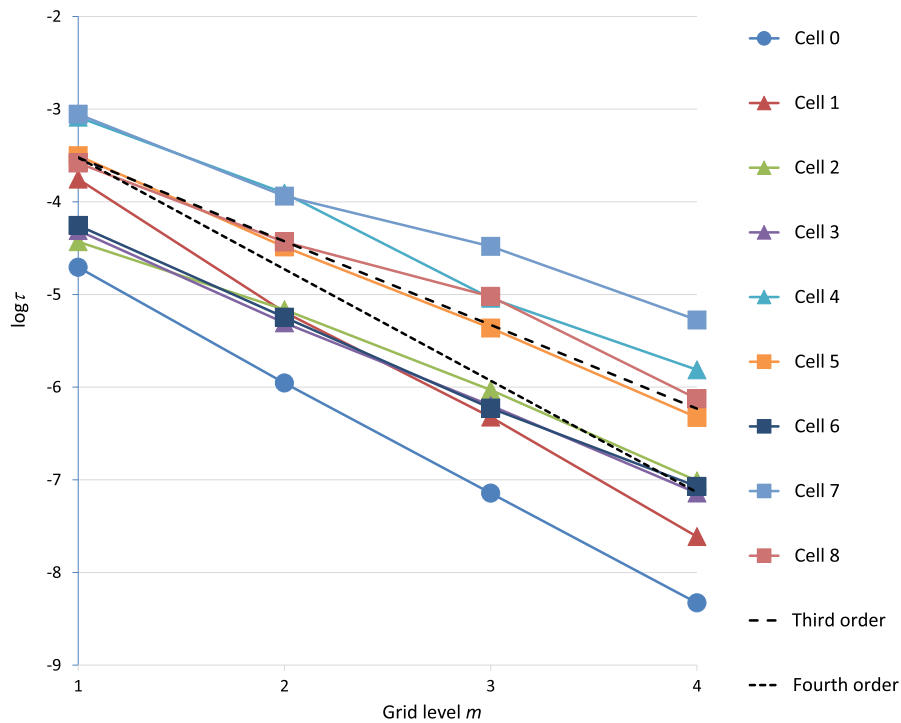

Fig. 11. Truncation error at the LCORE test cells.

Figs. 11 and 12 are plots of $\log(\tau_{i,j}^{(m)})$, $1 \le m \le 4$, for each of the 18 test cells (i, j) enumerated in Fig. 10, along with reference curves indicating third- and fourth-order convergence. The curves corresponding to test cells at block interiors, boundaries and corners are plotted with circular, triangular and square markers, respectively. The truncation error at the interior test cells is seen to converge at fourth-order as expected. Since all of the other test cells lie along block boundaries, we cannot anticipate greater than third-order convergence in general, yet most of those rates are close to fourth-order as well, including cell 8, which is adjacent to the X point.
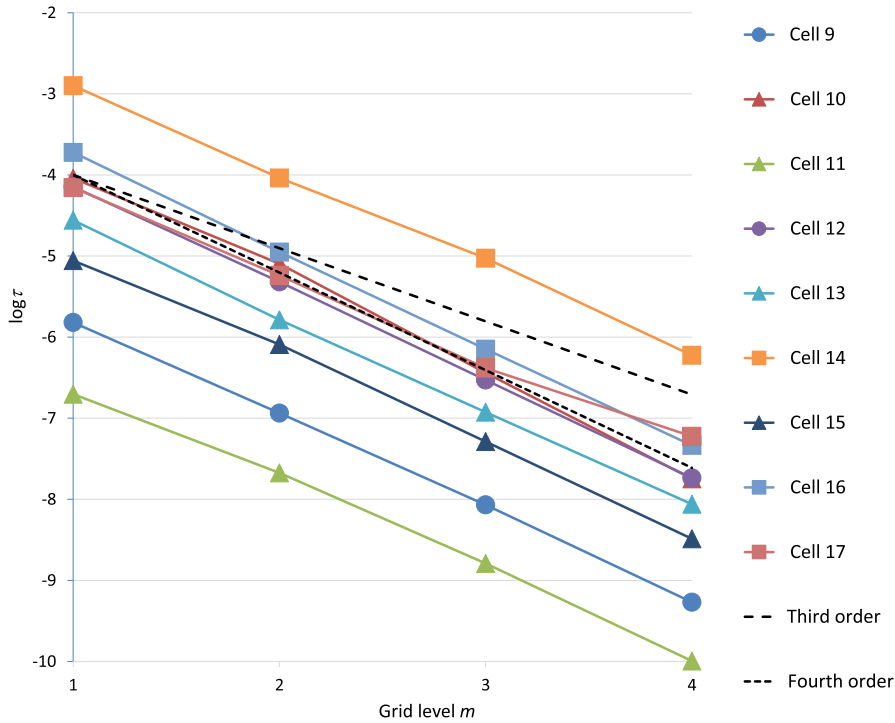
Fig. 12. Truncation error at the MCORE test cells.

The preceding results were generated using a mapping grid with 24 radial cells in the core blocks and 256 poloidal cells in the union of the core blocks (192 poloidal cells around the MCORE with 32 each in the LCORE and RCORE). The resolution of the LCSOL, RCSOL, LSOL, RSOL, LPF and RPF blocks was the same as that of LCORE and MCORE, and the resolution of the MCSOL block was the same as the MCORE block. The question arises as to how the mapping grid resolution affects the truncation error in tests like the one above. In the approach described in Section 4, the mapping grid nodes are constructed to lie on flux surfaces away from the X point. When the poloidal resolution of the computational grid is finer than that of the mapping grid, the B-spline interpolation used to evaluate the mapping at points not belonging to the set of mapping grid nodes is not guaranteed to yield intermediate points on flux surfaces. The exact cancellation of the magnetic flux in the calculation of (37b) will not occur, leading to the numerical pollution issue described at the end of Section 3.2. To investigate the magnitude of this effect, we plot in Fig. 13 the truncation error at a particular velocity space index and vary the poloidal mapping grid resolution from 32 to 512 poloidal cells by factors of two. To make the error reduction easier to see, the color map in these plots is saturated at a value of 2×10^{-8}. As the poloidal mapping resolution is increased, the pollution error is sufficiently reduced to observe the smooth error corresponding to the density gradient in the LCORE and RCORE blocks, indicated by the arrow in the bottom-most figure. In contrast to the emerging smooth error, oscillatory error is observed near the X point and the block boundaries containing it, which we have determined is related to the combination of the ray tracing and flux blending algorithms used in the construction of the discrete block mappings in the flux-dealigned region as described in Section 4. Although the nonsmoothness of this error could presumably be further reduced with additional effort, there is little point in doing so since it is ordered error nevertheless, as demonstrated by the results in Fig. 11, which include error measurements in cells (*i.e.*, 4, 7 and 8) located within this region.

Finally, in Fig. 14, we plot the truncation error at test cells 3 and 8 using the divergence-free velocity formulation described in Section 3.2 (solid lines) versus a non-divergence-free (albeit fourth-order accurate) velocity discretization employed in a calculation of fluxes via (11) rather than (10). We choose these two cells because they represent two extremes relative to similar comparisons using the other 16 test cells. Whereas the difference between the truncation errors at cell 3 is fairly small, more than an order of magnitude improvement is observed at cell 8 using the divergence-free formulation. Error reductions lying between these two cases are observed for the remaining test cells.

7. Summary

The predictive simulation of the edge plasma region of a tokamak fusion reactor via a continuum gyrokinetic model involves multiple components, including the accurate and efficient advection of plasma species distribution functions in phase space. We have described here our approach for the development and implementation of a conservative, high-order, MMB, finite-volume, spatial discretization of a full-f gyrokinetic Vlasov model in axisymmetric edge geometries.
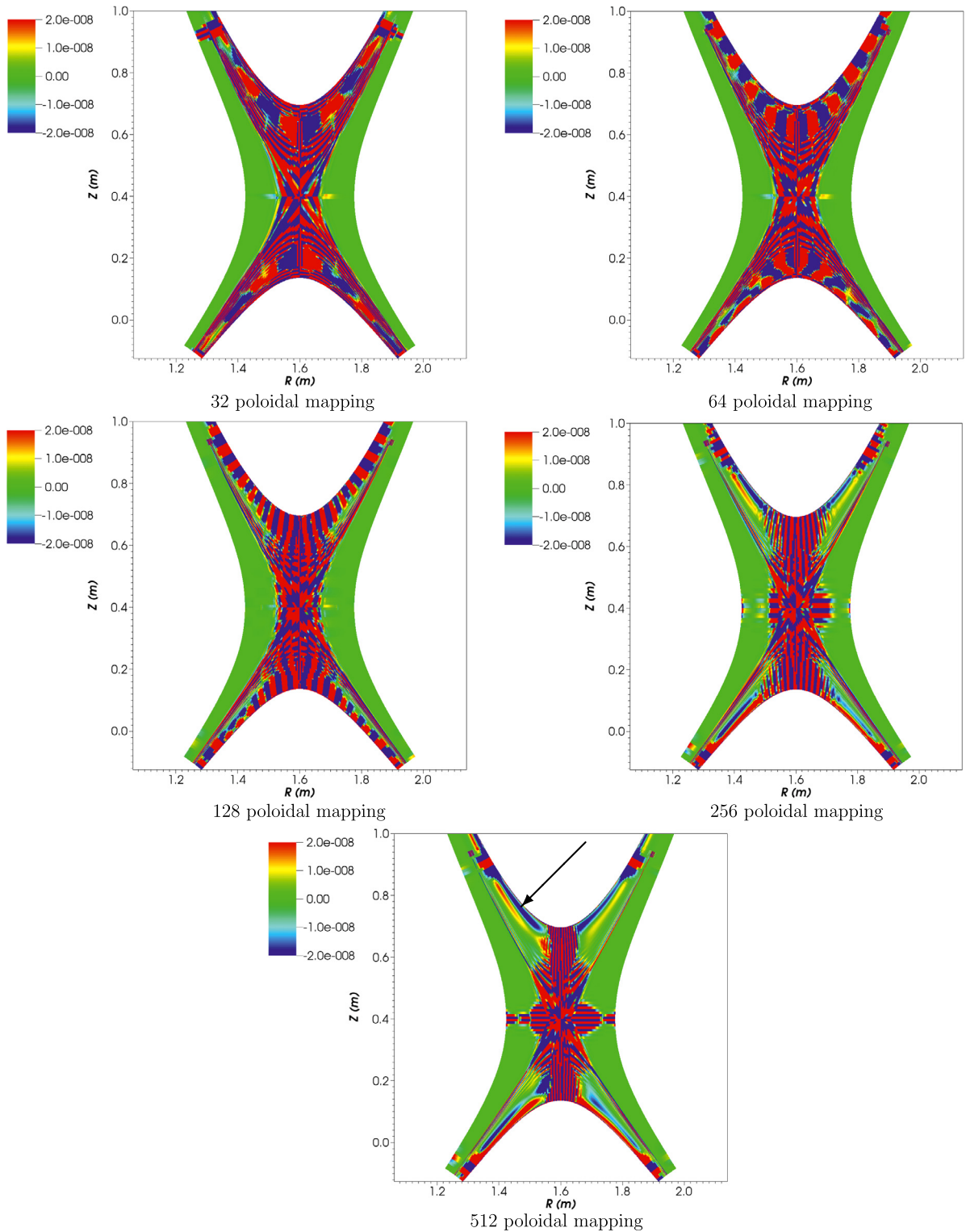
Fig. 13. Truncation error near the X point evaluated at a specified velocity space index as the poloidal mapping resolution is successively doubled from 32 to 512 cells. The arrow in the bottom-most plot indicates smooth truncation error associated with the density gradient, which emerges after the pollution error caused by field misalignment is sufficiently reduced.
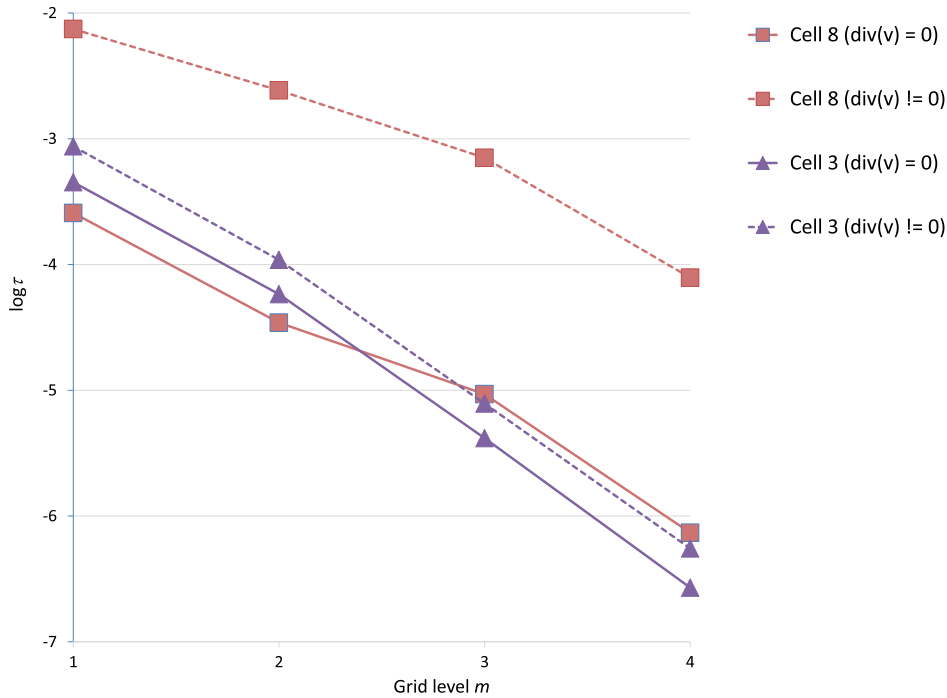
Fig. 14. Comparison of the truncation error at test cells 3 and 8 using the divergence-free velocity discretization (solid lines) versus a non-divergence-free discretization (dashed lines).

An important element of the approach is the discretization of the gyrokinetic phase space velocity, whose zero divergence property is preserved discretely to machine precision. This enables a conservative formulation of the gyrokinetic system without the accumulation of truncation error in long-time integration that would result from a merely asymptotically small velocity divergence. Furthermore, the discrete velocity contribution of parallel streaming (the dominant velocity component), ∇B drifts and curvature drifts are computed exactly from pointwise evaluations of the magnetic field data. Except for a configuration space volume factor (whose accurate calculation is required in any finite-volume discretization) in the acceleration terms, no metric factors appear in the velocity discretization, thereby eliminating the possibility of error contribution from their discretization, which is an important concern in mapped grid approaches [35]. The velocity discretization respects the asymptotic ordering of the gyrokinetic theory by eliminating the contribution of the zeroth-order parallel streaming term on phase space cell faces lying within flux surfaces, except near the X point where were a flux-aligned grid is precluded, leaving only the first-order drift terms to be computed without pollution from the lower-order terms.

We demonstrated the effectiveness of the approach on an analytically defined edge geometry including both sides of the magnetic separatrix. In addition to enabling the direct measurement of the spatial truncation error resulting from the combination of all algorithmic components, the use of Boltzmann equilibrium solutions (52) demonstrates an important advantage of our approach applied to the edge plasma problem. As described in Section 1, near a tokamak core, a common approximation is to represent distribution functions as perturbations of a zeroth-order distribution function, $f = f_0 + \delta f$, where f_0 is similar in form to (52). Since f_0 can be computed in the core, it can be explicitly removed from the model. Lacking a similar approach in the edge region, the accurate calculation of f_0 as an integral part of a full-f model is therefore important to ensure that its discretization error does not overwhelm the δf contribution of primary interest.

The spatial discretization described here is the foundation of a broader effort centered around the development of the COGENT code, which, as discussed in Section 5, also incorporates complementary algorithms for the treatment of collision operators, self-consistent electrostatic fields and high-order, semi-implicit time integration needed for a complete edge plasma simulation. To our knowledge, COGENT's ability to solve a continuum gyrokinetic model in edge geometries spanning both sides of the magnetic separatrix is unique. Our current and future work includes the relaxation of the assumption of toroidal symmetry in the development of a 5D capability for the simulation of edge turbulence.

Acknowledgements

Table 2
Primitive reference parameters.

$\widetilde{n}$	number density
$\widetilde{T}$	temperature
$\widetilde{L}$	length
$\widetilde{m}$	mass
$\widetilde{B}$	magnetic field

Table 3
Derived reference parameters.

$\widetilde{v} = (\widetilde{T}/\widetilde{m})^{1/2}$	thermal speed
$\widetilde{\tau} = \widetilde{L}/\widetilde{v}$	transit time
$\widetilde{\mu} = \widetilde{T}/(2\widetilde{B})$	magnetic moment
$\widetilde{f} = \widetilde{n}/(\pi\widetilde{v}^3)$	distribution function
$\widetilde{\Phi} = \widetilde{T}/e$	potential
$\widetilde{\Omega} = e\widetilde{B}/\widetilde{m}$	gyrofrequency
$\widetilde{\lambda}_D = (\epsilon_0\widetilde{T}/(\widetilde{n}e^2))^{1/2}$	Debye length

Table 4
Normalized gyrokinetic Vlasov–Poisson variables.

$\widehat{t} = t/\widetilde{\tau}$	time
$\widehat{v}_\parallel = v_\parallel/\widetilde{v}$	parallel velocity
$\widehat{n} = n/\widetilde{n}$	number density
$\widehat{m} = m/\widetilde{m}$	mass
$\widehat{f} = f/\widetilde{f}$	distribution function
$\widehat{T} = T/\widetilde{T}$	temperature
$\widehat{B} = B/\widetilde{B}$	magnetic field
$\widehat{\Phi} = \Phi/\widetilde{\Phi}$	potential
$\widehat{\mu} = \mu/\widetilde{\mu}$	magnetic moment

Table 5
Dimensionless gyrokinetic Vlasov–Poisson parameters.

$\rho_L = \widetilde{v}/(\widetilde{\Omega}\widetilde{L})$	Larmor number: ratio of gyroradius to scale length
$\lambda_D = \widetilde{\lambda}_D/\widetilde{L}$	Debye number: ratio of Debye length to scale length

Appendix A

A.1. Normalizations

Equations (1)–(3) and (48) are obtained from the gyrokinetic Vlasov–Poisson system derived in [22] using a normalization relative to a reference material and fields described by the primitive parameters specified in Table 2 and the derived quantities in Table 3. The normalized variables used in the gyrokinetic Vlasov–Poisson model are displayed in Table 4. In terms of the reference scales, two dimensionless numbers, defined in Table 5, appear in the normalized gyrokinetic Vlasov–Poisson system.

A.2. Gyrokinetic velocity divergence

Define $\mathbf{u} = (\mathbf{u_R}, u_{v_\parallel}) = (B_\parallel^*\dot{\mathbf{R}}, B_\parallel^*\dot{v}_\parallel)$. Letting $\mathbf{A}$ be such that $\mathbf{B} = \nabla_\mathbf{R} \times \mathbf{A}$ and defining p as in (14), we have from (2)–(3) that

$$\mathbf{u_R} = \nabla_\mathbf{R} \times \left\{ v_\parallel \left(\mathbf{A} + \frac{mv_\parallel\rho_L}{Z}\mathbf{b} \right) \right\} + \mathbf{b} \times \nabla_\mathbf{R}p, \tag{57a}$$

$$u_{v_\parallel} = -\nabla_\mathbf{R} \times \left(\frac{Z}{m\rho_L}\mathbf{A} + v_\parallel\mathbf{b} \right) \cdot \nabla_\mathbf{R}p. \tag{57b}$$

Therefore,

$$\nabla_{\mathbf{R}} \cdot \mathbf{u}_{\mathbf{R}} = \nabla_{\mathbf{R}} \cdot (\mathbf{b} \times \nabla_{\mathbf{R}} p) \tag{58}$$
$$= \nabla_{\mathbf{R}} p \cdot (\nabla_{\mathbf{R}} \times \mathbf{b}) - \mathbf{b} \cdot (\nabla_{\mathbf{R}} \times \nabla_{\mathbf{R}} p)$$
$$= \nabla_{\mathbf{R}} p \cdot (\nabla_{\mathbf{R}} \times \mathbf{b}),$$

and

$$\frac{\partial u_{v_\parallel}}{\partial v_\parallel} = -(\nabla_{\mathbf{R}} \times \mathbf{b}) \cdot \nabla_{\mathbf{R}} p, \tag{59}$$

from which (4) follows.

A.3. Face integrals

In direction 1, the face integral (18) for $\alpha = 0$ or 1 is evaluated as:

$$\int_{\mathbf{X}(V_1^\alpha)} \boldsymbol{\sigma} = \tag{60}$$

$$\int_{V_1^\alpha} \left(\widetilde{u}_3 \det \begin{vmatrix} \frac{\partial \mathbf{X}_0}{\partial \xi_0} & \frac{\partial \mathbf{X}_0}{\partial \xi_2} & \frac{\partial \mathbf{X}_0}{\partial \xi_3} \\ \frac{\partial \mathbf{X}_1}{\partial \xi_0} & \frac{\partial \mathbf{X}_1}{\partial \xi_2} & \frac{\partial \mathbf{X}_1}{\partial \xi_3} \\ \frac{\partial \mathbf{X}_2}{\partial \xi_0} & \frac{\partial \mathbf{X}_2}{\partial \xi_2} & \frac{\partial \mathbf{X}_2}{\partial \xi_3} \end{vmatrix} \right)_{\xi_1 = \xi_1^\alpha} d\xi_0 d\xi_2 d\xi_3 - \int_{V_1^\alpha} \left(\widetilde{u}_2 \det \begin{vmatrix} \frac{\partial \mathbf{X}_0}{\partial \xi_0} & \frac{\partial \mathbf{X}_0}{\partial \xi_2} & \frac{\partial \mathbf{X}_0}{\partial \xi_3} \\ \frac{\partial \mathbf{X}_1}{\partial \xi_0} & \frac{\partial \mathbf{X}_1}{\partial \xi_2} & \frac{\partial \mathbf{X}_1}{\partial \xi_3} \\ \frac{\partial \mathbf{X}_3}{\partial \xi_0} & \frac{\partial \mathbf{X}_3}{\partial \xi_2} & \frac{\partial \mathbf{X}_3}{\partial \xi_3} \end{vmatrix} \right)_{\xi_1 = \xi_1^\alpha} d\xi_0 d\xi_2 d\xi_3$$

$$+ \int_{V_1^\alpha} \left(\widetilde{u}_1 \det \begin{vmatrix} \frac{\partial \mathbf{X}_0}{\partial \xi_0} & \frac{\partial \mathbf{X}_0}{\partial \xi_2} & \frac{\partial \mathbf{X}_0}{\partial \xi_3} \\ \frac{\partial \mathbf{X}_2}{\partial \xi_0} & \frac{\partial \mathbf{X}_2}{\partial \xi_2} & \frac{\partial \mathbf{X}_2}{\partial \xi_3} \\ \frac{\partial \mathbf{X}_3}{\partial \xi_0} & \frac{\partial \mathbf{X}_3}{\partial \xi_2} & \frac{\partial \mathbf{X}_3}{\partial \xi_3} \end{vmatrix} \right)_{\xi_1 = \xi_1^\alpha} d\xi_0 d\xi_2 d\xi_3 - \int_{V_1^\alpha} \left(\widetilde{u}_0 \det \begin{vmatrix} \frac{\partial \mathbf{X}_1}{\partial \xi_0} & \frac{\partial \mathbf{X}_1}{\partial \xi_2} & \frac{\partial \mathbf{X}_1}{\partial \xi_3} \\ \frac{\partial \mathbf{X}_2}{\partial \xi_0} & \frac{\partial \mathbf{X}_2}{\partial \xi_2} & \frac{\partial \mathbf{X}_2}{\partial \xi_3} \\ \frac{\partial \mathbf{X}_3}{\partial \xi_0} & \frac{\partial \mathbf{X}_3}{\partial \xi_2} & \frac{\partial \mathbf{X}_3}{\partial \xi_3} \end{vmatrix} \right)_{\xi_1 = \xi_1^\alpha} d\xi_0 d\xi_2 d\xi_3$$

$$= \int_{V_1^\alpha} \left(\widetilde{u}_3 \det \begin{vmatrix} 1 & 0 & 0 \\ 0 & \frac{\partial \mathbf{X}_1}{\partial \xi_2} & \frac{\partial \mathbf{X}_1}{\partial \xi_3} \\ 0 & \frac{\partial \mathbf{X}_2}{\partial \xi_2} & \frac{\partial \mathbf{X}_2}{\partial \xi_3} \end{vmatrix} \right)_{\xi_1 = \xi_1^\alpha} d\xi_0 d\xi_2 d\xi_3 - \int_{V_1^\alpha} \left(\widetilde{u}_2 \det \begin{vmatrix} 1 & 0 & 0 \\ 0 & \frac{\partial \mathbf{X}_1}{\partial \xi_2} & \frac{\partial \mathbf{X}_1}{\partial \xi_3} \\ 0 & \frac{\partial \mathbf{X}_3}{\partial \xi_2} & \frac{\partial \mathbf{X}_3}{\partial \xi_3} \end{vmatrix} \right)_{\xi_1 = \xi_1^\alpha} d\xi_0 d\xi_2 d\xi_3$$

$$+ \int_{V_1^\alpha} \left(\widetilde{u}_1 \det \begin{vmatrix} 1 & 0 & 0 \\ 0 & \frac{\partial \mathbf{X}_2}{\partial \xi_2} & \frac{\partial \mathbf{X}_2}{\partial \xi_3} \\ 0 & \frac{\partial \mathbf{X}_3}{\partial \xi_2} & \frac{\partial \mathbf{X}_3}{\partial \xi_3} \end{vmatrix} \right)_{\xi_1 = \xi_1^\alpha} d\xi_0 d\xi_2 d\xi_3 - \int_{V_1^\alpha} \left(\widetilde{u}_0 \det \begin{vmatrix} 0 & \frac{\partial \mathbf{X}_1}{\partial \xi_2} & \frac{\partial \mathbf{X}_1}{\partial \xi_3} \\ 0 & \frac{\partial \mathbf{X}_2}{\partial \xi_2} & \frac{\partial \mathbf{X}_2}{\partial \xi_3} \\ 0 & \frac{\partial \mathbf{X}_3}{\partial \xi_2} & \frac{\partial \mathbf{X}_3}{\partial \xi_3} \end{vmatrix} \right)_{\xi_1 = \xi_1^\alpha} d\xi_0 d\xi_2 d\xi_3$$

$$= \int_{V_1^\alpha} \left(\widetilde{u}_3 N_{1,3}^T + \widetilde{u}_2 N_{1,2}^T + \widetilde{u}_1 N_{1,1}^T \right)_{\xi_1 = \xi_1^\alpha} d\xi_0 d\xi_2 d\xi_3$$

$$= \int_{V_1^\alpha} \left(\mathbf{N}^T \widetilde{\mathbf{u}} \right)_1 d\mathbf{V}_{\boldsymbol{\xi}}.$$

The integrals (18) in the other directions are obtained similarly.

A.4. Identification of the skew-symmetric tensor used in the gyrokinetic velocity discretization

To find a skew-symmetric, second-order tensor satisfying (20)–(21), we note that 4-vectors of the form $(0, \nabla_{\boldsymbol{R}} \times \mathbf{v})$ with $\mathbf{v} = (v_1, v_2, v_3)$ are trivially expressible as a skew-symmetric tensor divergence:

$$(0, \nabla_{\boldsymbol{R}} \times \mathbf{v})_j = \sum_{j'=0}^{3} \frac{\partial \eta_{j,j'}}{\partial x_{j'}}, \quad 0 \le j \le 3, \tag{61}$$

where

$$\eta = \begin{pmatrix} 0 & 0 & 0 & 0 \\ 0 & 0 & v_3 & -v_2 \\ 0 & -v_3 & 0 & v_1 \\ 0 & v_2 & -v_1 & 0 \end{pmatrix}. \tag{62}$$

We therefore separate the terms of (2) involving $\mathbf{B} = \nabla_{\mathbf{R}} \times \mathbf{A}$ and $\nabla_{\mathbf{R}} \times \mathbf{b}$, resulting in a decomposition $\widetilde{\mathbf{u}} = \widetilde{\mathbf{u}}_1 + \widetilde{\mathbf{u}}_2$, where

$$\widetilde{\mathbf{u}}_1 = \left(0, \nabla_{\mathbf{R}} \times \left[v_{\|} \left(\mathbf{A} + \frac{m v_{\|} \rho_L}{Z} \mathbf{b} \right) \right] \right), \tag{63a}$$

$$\widetilde{\mathbf{u}}_2 = \left(-v_{\|} (\nabla_{\mathbf{R}} \times \mathbf{b}) \cdot \nabla_{\mathbf{R}} p, \, \mathbf{b} \times \nabla_{\mathbf{R}} p \right). \tag{63b}$$

The entries $\omega_{i,j}$, $1 \le i < j \le 3$, given by (22b)–(22d) are then obtained from $\widetilde{\mathbf{u}}_1$. We obtain the contribution from $\widetilde{\mathbf{u}}_2$ by setting $\omega_{0,j} = (-1)^{j+1} v_{\|} (\mathbf{b} \times \nabla_{\mathbf{R}} p)_j$, $1 \le j \le 3$, since, using (21) and (58),

$$\nabla_{\mathbf{R}} \cdot (\zeta_{0,1}, \zeta_{0,2}, \zeta_{0,3}) = \nabla_{\mathbf{R}} \cdot (-\omega_{0,1}, \omega_{0,2}, -\omega_{0,3}) = -v_{\|} (\nabla_{\mathbf{R}} \times \mathbf{b}) \cdot \nabla_{\mathbf{R}} p, \tag{64a}$$

$$\frac{\partial}{\partial v_{\|}} (\zeta_{0,1}, \zeta_{0,2}, \zeta_{0,3}) = \frac{\partial}{\partial v_{\|}} (-\omega_{0,1}, \omega_{0,2}, -\omega_{0,3}) = \mathbf{b} \times \nabla_{\mathbf{R}} p. \tag{64b}$$

A.5. An inequality used in the construction of mapping grids

In the derivation of (46), assuming that $b \ne 0$ and $b^2 > 4ac$, we have

$$\left[b^2 - 2c(a - c) \right]^2 - \left[2c\sqrt{b^2 + (a - c)^2} \right]^2 = b^2 (b^2 - 4ac) > 0, \tag{65}$$

so

$$2|c|\sqrt{b^2 + (a - c)^2} < \left| b^2 - 2c(a - c) \right|. \tag{66}$$

However,

$$b^2 - 2c(a - c) > 0, \tag{67}$$

since, if $ac \le 0$, (67) is verified trivially; otherwise

$$b^2 - 2c(a - c) = b^2 - 2ac + 2c^2 > b^2 - 4ac + 2c^2 > 0. \tag{68}$$

Therefore, using (66),

$$-2c\sqrt{b^2 + (a - c)^2} \le 2|c|\sqrt{b^2 + (a - c)^2} < b^2 - 2c(a - c), \tag{69}$$

yielding

$$b^2 + 2c(-a + \sqrt{b^2 + (a - c)^2} + c) > 0. \tag{70}$$

A.6. Boltzmann equilibrium

With the definitions (52)–(54) and

$$w = \pi^{-1/2} (2T/m)^{-3/2} \exp\left(-\frac{m v_{\|}^2 + \mu B(\psi, \theta)}{2T} \right), \tag{71}$$

we have

$$\nabla f = w \left(-\frac{n\mu}{2T} \nabla B + \nabla n \right), \tag{72a}$$

$$\partial_{v_{\|}} f = -w \frac{m v_{\|} n}{T}, \tag{72b}$$

$$\nabla \phi = -\frac{T}{Zn} \nabla n. \tag{72c}$$

Since $\mathbf{B} \cdot \nabla n = \mathbf{B} \cdot \nabla \phi = 0$, we have

$$\mathbf{B}^* \cdot \nabla f = w \left[-\frac{n\mu}{2T} \mathbf{B} \cdot \nabla B + \rho_L \frac{m v_{\|}}{Z} (\nabla \times \mathbf{b}) \cdot \left(-\frac{n\mu}{2T} \nabla B + \nabla n \right) \right], \tag{73a}$$

$$\mathbf{B}^* \cdot \mathbf{G} = \frac{\mu}{2} \mathbf{B} \cdot \nabla B - \rho_L \frac{m v_{\|}}{Z} (\nabla \times \mathbf{b}) \cdot \left(\frac{T}{n} \nabla n - \frac{\mu}{2} \nabla B \right), \tag{73b}$$

and hence

$$\mathbf{B}^* \cdot \left(v_{\|} \nabla f + w \frac{v_{\|} n}{T} \mathbf{G} \right) = 0. \tag{74}$$

Also,

$$\mathbf{G} \times \nabla f = w\left[\frac{\mu}{2}\nabla n \times \nabla B - \frac{T}{n}\nabla n \times \nabla n - \frac{n\mu^2}{4T}\nabla B \times \nabla B + \frac{\mu}{2}\nabla B \times \nabla n\right] = 0. \tag{75}$$

Therefore,

$$\begin{aligned} B_\parallel^*\left(\dot{\mathbf{R}}\cdot\nabla f + \dot{v}_\parallel\partial_{v_\parallel}f\right) &= \mathbf{B}^*\cdot\left(v_\parallel\nabla f + w\frac{v_\parallel n}{T}\mathbf{G}\right) + \frac{\rho_L}{2}\left(\mathbf{b}\times\mathbf{G}\right)\cdot\nabla f \\ &= \frac{\rho_L}{2}\left(\mathbf{G}\times\nabla f\right)\cdot\mathbf{b} \\ &= 0. \end{aligned} \tag{76}$$

Since the gyrokinetic velocity is divergence free (Appendix A.2),

$$\nabla\cdot\left(\dot{\mathbf{R}}B_\parallel^*f\right) + \frac{\partial}{\partial v_\parallel}\left(\dot{v}_\parallel B_\parallel^* f\right) = 0. \tag{77}$$

References

[1] www.euro-fusion.org.
[2] en.wikipedia.org/wiki/Differential_form.
[3] en.wikipedia.org/wiki/Polyharmonic_spline.
[4] J. Candy, Gyro, fusion.gat.com/comp/parallel/.
[5] J. Candy, R.E. Waltz, Anomalous transport in the DIII-D tokamak matched by supercomputer simulation, Phys. Rev. Lett. 91 (4) (2003) 045001.
[6] J. Candy, R.E. Waltz, An Eulerian gyrokinetic-Maxwell solver, J. Comput. Phys. 186 (2003) 545–581.
[7] C.S. Chang, S. Ku, P.H. Diamond, Z. Lin, S. Parker, T.S. Hahm, N. Samatova, Compressed ion temperature gradient turbulence in diverted tokamak edge, Phys. Plasmas 16 (2009) 056108.
[8] P. Colella, M.R. Dorr, J.A.F. Hittinger, D.F. Martin, High-order, finite-volume methods in mapped coordinates, J. Comput. Phys. 230 (2011) 2952–2976.
[9] P. Colella, D.T. Graves, T.J. Ligocki, D.F. Martin, D. Modiano, D.B. Serafini, B. Van Straalen, Chombo software package for AMR applications – Design document, seesar.lbl.gov/anag/chombo.
[10] M. Dorf, R. Cohen, M. Dorr, T. Rognlien, J. Hittinger, J. Compton, P. Colella, D. Martin, P. McCorquodale, Simulation of neoclassical transport with the continuum gyrokinetic code COGENT, Phys. Plasmas 20 (2013) 012513.
[11] M. Dorf, M. Dorr, J. Hittinger, W. Lee, D. Ghosh, Conservative high-order finite-volume modeling of drift waves, J. Comput. Phys. 373 (2018) 446–454, https://doi.org/10.1016/j.jcp.2018.07.009.
[12] M.A. Dorf, R.H. Cohen, J.C. Compton, M. Dorr, T.D. Rognlien, J. Angus, S. Krasheninnikov, P. Colella, D. Martin, P. McCorquodale, Progress with the COGENT edge kinetic code: collision operator options, Contrib. Plasma Phys. 52 (5–6) (2012) 518–522.
[13] M.A. Dorf, R.H. Cohen, M. Dorr, J. Hittinger, T.D. Rognlien, Progress with the COGENT edge kinetic code: implementing the Fokker–Planck collision operator, Contrib. Plasma Phys. 54 (4–6) (2014) 517–523.
[14] M.A. Dorf, R.H. Cohen, M. Dorr, T. Rognlien, J. Hittinger, J. Compton, P. Colella, D. Martin, P. McCorquodale, Numerical modelling of geodesic acoustic mode relaxation in a tokamak edge, Nucl. Fusion 53 (2013) 063015.
[15] M.A. Dorf, M.R. Dorr, J.A. Hittinger, R.H. Cohen, T.D. Rognlien, Continuum kinetic modeling of the tokamak plasma edge, Phys. Plasmas 23 (2016) 056102.
[16] W. Dorland, F. Jenko, M. Kotschenreuther, B.N. Rogers, Electron temperature gradient turbulence, Phys. Rev. Lett. 85 (2000) 5579.
[17] M.R. Dorr, R.H. Cohen, P. Colella, M.A. Dorf, J.A.F. Hittinger, D.F. Martin, Numerical simulation of phase space advection in gyrokinetic models of fusion plasmas, in: Proceedings of SciDAC 2010, Chattanooga, TN, July 2010.
[18] D. Ghosh, M.A. Dorf, M.R. Dorr, J.A.F. Hittinger, Kinetic simulation of collisional magnetized plasmas with semi-implicit time integration, SIAM J. Sci. Comput. (2018), https://doi.org/10.1007/s10915-018-0726-6, in press, https://link.springer.com/article/10.1007%2Fs10915-018-0726-6.
[19] D. Ghosh, M.A. Dorf, J. Hittinger, M. Dorr, Implicit–explicit time integration for the Vlasov–Fokker–Planck equations, in: Proceedings of the 48th AIAA Plasmadynamics and Lasers Conference, American Institute of Aeronautics and Astronautics, June 2017, pp. 5–9.
[20] F.X. Giraldo, J.F. Kelly, E.M. Constantinescu, Implicit–explicit formulations of a three-dimensional nonhydrostatic unified model of the atmosphere (NUMA), SIAM J. Sci. Comput. 35 (5) (2013) B1162–B1194.
[21] V. Grandgirard, Y. Sarazin, P. Angelino, A. Bottino, N. Crouseilles, G. Darmet, G. Dif-Pradalier, X. Garbet, Ph. Ghendrih, S. Jolliet, G. Latu, E. Sonnendrücker, L. Villard, Global full-f gyrokinetic simulations of plasma turbulence, Plasma Phys. Control. Fusion 49 (2007) B173–B182.
[22] T.S. Hahm, Nonlinear gyrokinetic equations for turbulence in core transport barriers, Phys. Plasmas 3 (12) (1996) 4658–4664.
[23] R.D. Hazeltine, J.D. Meiss, Plasma Confinement, Addison-Wesley Publishing Company, Redwood City, CA, 1992.
[24] J.A. Heikkinen, S.J. Janhunen, T.P. Kiviniemi, F. Ogando, Full-f gyrokinetic method for particle simulation of tokamak transport, J. Comput. Phys. 227 (2008) 5582–5609.
[25] J.A.F. Hittinger, J.W. Banks, Block-structured adaptive mesh refinement algorithms for Vlasov simulation, J. Comput. Phys. 241 (2013) 118–140.
[26] Y. Idomura, Full-f gyrokinetic simulation over a confinement time, Phys. Plasmas 21 (2007) 022517.
[27] Y. Idomura, A new hybrid kinetic electron model for full-f gyrokinetic simulations, J. Comput. Phys. 313 (2016) 511–531.
[28] S.J. Janhunen, T.P. Kiviniemi, J.A. Heikkinen, T. Korpilo, S. Leerink, M. Nora, F. Ogando, Recent advances in gyrokinetic full-f particle simulation of medium sized tokamaks with ELMFIRE, Contrib. Plasma Phys. 50 (3–5) (2010) 252–255.
[29] F. Jenko, Massively parallel Vlasov simulation of electromagnetic drift-wave turbulence, Comput. Phys. Commun. 125 (2000) 196.
[30] F. Jenko, T. Dannert, C. Angioni, Heat and particle transport in a tokamak: advances in nonlinear gyrokinetics, Plasma Phys. Control. Fusion 47 (2005) B195.
[31] G.-S. Jiang, C.-W. Shu, Efficient implementation of weighted ENO schemes, J. Comput. Phys. 126 (1) (1996) 202–228.
[32] C.A. Kennedy, M.H. Carpenter, Additive Runge–Kutta schemes for convection–diffusion–reaction equations, Appl. Numer. Math. 44 (1–2) (2003) 139–181.
[33] K. Kim, C.S. Chang, J. Seo, S. Ku, W. Choe, What happens to full-f gyrokinetic transport and turbulence in a toroidal wedge simulation?, Phys. Plasmas 24 (2017) 012306.

[34] T.P. Kiviniemi, J.A. Heikkinen, S. Janhunen, S.V. Henriksson, Full f gyrokinetic simulation of ft-2 tokamak plasma, Plasma Phys. Control. Fusion 48 (2006) A327–A333.

[35] D.A. Kopriva, Metric identities and the discontinuous spectral element method on curvilinear meshes, SIAM J. Sci. Comput. 26 (3) (2006) 301–327.

[36] M. Kotschenreuther, G. Rewoldt, W.M. Tang, Comparison of initial value and eigenvalue codes for kinetic toroidal plasma instabilities, Comput. Phys. Commun. 88 (128) (1995).

[37] S. Ku, C.S. Chang, P.H. Diamond, Full-f gyrokinetic particle simulation of centrally heated global ITG turbulence from magnetic axis to edge pedestal top in a realistic tokamak geometry, Nucl. Fusion 49 (2009) 115021.

[38] P. McCorquodale, M.R. Dorr, J.A.F. Hittinger, P. Colella, High-order finite-volume methods for hyperbolic conservation laws on mapped multiblock grids, J. Comput. Phys. 288 (2015).

[39] G.D. Porter, R. Isler, J. Boedo, T.D. Rognlien, Detailed comparison of simulated and measured plasma profiles in the scrape-off layer and edge plasma of DIII-D, Phys. Plasmas 7 (9) (2000) 3663–3680.

[40] T.D. Rognlien, M.E. Rensink, Edge-plasma models and characteristics for magnetic fusion energy devices, Fusion Eng. Des. 60 (2002) 497.

[41] T.D. Rognlien, D.D. Ryutov, N. Mattor, G.D. Porter, Two-dimensional electric fields and drifts near the magnetic separatrix in divertor tokamaks, Phys. Plasmas 6 (1999) 1851.

[42] T.D. Rognlien, J.L. Milovich, M.E. Rensink, G.D. Porter, A fully implicit, time dependent 2-d fluid code for modeling tokamak edge plasmas, J. Nucl. Mater. 196–198 (C) (1992) 347–351.

[43] Michael Spivak, Calculus on Manifolds, W.A. Benjamin, Inc., New York, NY, 1965.

[44] M.V. Umansky, M.S. Day, T.D. Rognlien, On numerical solution of strongly anisotropic diffusion equation on misaligned grids, Numer. Heat Transf., Part B, Fundam. 47 (2005) 533–554.

[45] S. Wiesen, D. Reiter, V. Kotov, M. Baelmans, W. Dekeyser, A.S. Kukushkin, S.W. Lisgo, R.A. Pitts, V. Rozhansky, G. Saibene, I. Veselova, S. Voskoboynikov, The new SOLPS-ITER code package, J. Nucl. Mater. 463 (2015) 480–484.